Optimizing functional properties of Mg-nanoferrite by varying thermal annealing time

Next Materials 13 (2026) 103601

Contents lists available at ScienceDirect

Next Materials

journal homepage: www.sciencedirect.com/journal/next-materials

Research article

Optimizing functional properties of Mg-nanoferrite by varying thermal annealing time

S.S. Modak [a], P. Tiwari [b], V.R. Reddy [c], M. Coïsson [e], P. Tiberto [d], L. Hashmi [d], F. Celegato [d], G. Barrera [d], Shailesh I. Kundalwal [e], F. Mazaleyrat [f], S.N. Kane [a,*]

[a] School of Physics, Devi Ahilya University, Indore, 452001, India
[b] Prestige Institute of Engineering Management and Research, Indore, 452010, India
[c] UGC-DAE Consortium for Scientific Research, Indore, 452001, India
[d] Istituto Nazionale di Ricerca Metrologica (INRIM), Strada delle Cacce 91, Torino, TO, 10135, Italy
[e] Department of Mechanical Engineering, Indian Institute of Technology Indore, Indore, India
[f] SATIE CNRS UMR 8029 Ecole Normale Superieure Paris-Saclay, University Paris-Saclay, 4 Avenue des sciences, Gif-sur-Yvette, 91190, France

ARTICLE INFO

Keywords:
XRD
Spinel-ferrites
Dielectric properties
Mössbauer-Spectroscopy
Magnetic-Properties

ABSTRACT

This study explores influence of duration of thermal-treatment for tuning structural,magnetic,dielectric response of nano-$MgFe_2O_4$ produced via sol-gel-auto-ignition. XRD(X-ray-diffraction) confirms nano-crystalline-spinel-phase growth, grain sizes ranging from 25.3 to 49.3 nm following annealing at 500 °C for 1–3 h. Structural analysis reveals a non-monotonic variation in lattice parameter, and progressive grain growth. Magnetic characterization indicates enhanced A-A, A-B super-exchange-interaction, weakened B-B exchange, leading to decreased Néel magnetic moment. Cation redistribution shows, increased Mg^{2+} and reduced Fe^{3+} at the B-site, altering the oxygen positional parameter and inversion degree. EDS validates that Fe,Mg,O are present in the studied samples. SEM images confirm particle-aggregation, irregular size- dispersal of particles, owing to samples' magnetic-nature. Mössbauer spectroscopy reveals two magnetic-sextets corresponding to Fe^{3+}-ions at A,B-sites, with isomer shift values confirming the +3 oxidation state. A non-magnetic doublet (~23%) is attributed to a spin-disordered shell region. Frequency-dependent-dielectric-measurements show decreasing dielectric-constant (ε',ε''),losses, while AC-conductivity(σ_{ac}) increases notably, follows power-law behavior. Impedance-analysis clearly show grain-boundaries govern dielectric-response at high frequencies. The Nyquist plot analysis reveals fitted equivalent-circuit parameters (grain resistance R_g and grain-boundary resistance R_{gb}) that decrease progressively with annealing time, confirming improved charge transport across grain boundaries. The thermal annealing time–controlled evolution of structural,magnetic,dielectric properties indicates the suitability of Mg nanoferrites for microwave-device-applications.

1. Introduction

Ferrimagnetic spinel-nanoferrites form a versatile family of materials that are valued by a wide array of advanced applications, including radiofrequency technologies, high-density-storage-devices, photo-catalysis, water-remediation, biomedical-applications [1–8]. Key factors such as the compositional-modifications, synthesis-protocol, by introducing metal-ions(e.g.-Mg,Zn,Ni), annealing conditions, cationic-distribution,grain-size must be carefully optimized [9,10] to enhance their properties, thereby expanding their utility in various domains. Among these, Mg-ferrites have gained considerable attention, particularly for their biocompatibility, low-toxicity, makes them an ideal candidate for bio-medical-uses [11,12]. Mg-nanoferrites exhibits partly-inverted-spinel-structure, wherein Mg^{2+},Fe^{3+} are present with an unequal distribution on A, B sites [1,13]. Studies showed that the distribution of cations in Mg-nanoferrites can be tuned by using suitable synthesis parameters [13,14]. Extensive studies on Zn, Co–Zn, Ni, Ni–Zn, Mn, Mn–Zn, and Mg ferrites have established that synthesis reaction temperature [15], cation substitution [16–18], post-synthesis thermal treatment [19–22], pH conditions [22], temperature-dependent magnetic properties [23], and ion irradiation [24–30] markedly influenced by their structural evolution. These factors

* Corresponding author.
E-mail address: kane_sn@yahoo.com (S.N. Kane).

https://doi.org/10.1016/j.nxmate.2026.103601
Received 23 May 2026; Received in revised form 15 September 2026; Accepted 17 September 2026
Available online 21 September 2026

induce changes in crystallinity, cationic-redistribution between tetrahedral(A),octahedral(B)-sites, thereby tunes their structural, magnetic, and dielectric properties of ferrites [22]. Structural-modifications get reflected in variations of oxygen positional parameters, grain size [25,27], inversion degree, lattice parameters, and magnetic interactions.

However, the existing literature primarily reports studies focused on post-synthesis thermal treatments employing different annealing temperatures to tune structural, magnetic, and dielectric properties through cationic redistribution [13–34]. Comparatively, limited attention has been paid to investigations in which annealing is carried out at a fixed temperature for varying durations, despite the potential of annealing time to induce optimized modifications in structural and magnetic behavior. Unlike temperature-variable studies that alter multiple thermodynamic parameters simultaneously, a fixed-temperature time--variable approach uniquely isolates the kinetic evolution of grain growth, cation site redistribution, and defect annealing, thereby enabling controlled tuning of functional properties without changing the activation energy landscape. In this context, present work examines annealing-time-dependence of structural,magnetic,dielectric-properties of $MgFe_2O_4$ system. A comprehensive correlation among these properties is established using Scanning Electron Microscopy, EDS: Energy Dispersive Spectroscopy, structural, magnetic, Mössbauer, dielectric, and impedance spectroscopy data. Recent advances in dopant engineering of spinel ferrites have demonstrated that carefully selected substitutions lead to distinct property enhancements. For instance, Sulamani et al. explored the impact of Zn ferrite and carbon dots on structural, morphological, and magnetic properties [35]. Farooq et al. studied chromium-substituted cadmium post-spinel ferrites [36]. Batool et al. reported on $Li_{0.5}Ce_xFe_{2.55\times}O_4$ ferrite systems [37]. GM et al. investigated Cd-substituted $CrCd_xFe_{15\times}O_3$ ferrites [38]. Irfan et al. explored n-doped Cd–Mg spinel ferrites with composition $Cd_{0.55\times}Mg_{0.5}Zn_xFe_2O_4$ [39]. Furthermore, Ga doping has been shown to significantly affect spinel ferrite properties [40]. These studies collectively underscore the importance of dopant choice in governing functional properties. In the present study, the focus is on pure $MgFe_2O_4$ where the annealing duration itself acts as the tuning parameter, offering a synthesis-independent route to property optimization. A dedicated comparison of the present study with recent literature on annealing-time and annealing-temperature-dependent $MgFe_2O_4$ ferrites is provided in the form of Table 1, clearly highlighting the novelty of the fixed-temperature, variable-time approach.

2. Experimental details

Mg-ferrite($MgFe_2O_4$) were made through sol-gel-auto-ignition, taking AR-grade-acetates-citrates-nitrates, with pH7, metal-salt:fuel-ratio 1:1. Further heating of mix at ~ 110 ℃ gives dry-gel (referred as M0 in figures and tables). Prepared dry gel samples were subjected to isothermal treatment in air at 500 ℃, for 1, 2 and 3 h (referred as M1, M2, M3 in figures and tables) respectively. Room temperature XRD-data was acquired by diffractometer(D2-Phaser), that used Cu-Kα-radiation:λ-0.15418 nm, analysis by MAUD(Materials-Analysis-Using-Diffraction)-software [42] gave lattice-parameter(a_{exp}),x-ray-density(ρ_{xrd}) [43]. W-H:(Williamson-Hall) method [44] gives grain-diameter ($D_{W\text{-}H}$), strain. Dislocation density (ρ_D), specific-surface-area(S), obtained by $D_{W\text{-}H}$ [45]. Scanning electron microscopy (SEM) and coupled with energy-dispersive X-ray spectroscopy (EDS) was employed to examine the surface morphology and elemental composition, respectively, while particle-size distributions were determined using ImageJ software [46]. High-resolution transmission electron microscopy (HRTEM) in copulation with EDS was further employed to examine the nanoscale morphology, elemental composition at nanoscale and lattice fringes, with selected-area electron diffraction (SAED) analysis used to confirm the crystalline nature and phase structure of the samples. Constant-acceleration-mode-Mössbauer-spectra taken at room-temperature, utilizing ^{57}Co:Rh source, using α-Fe-calibration. Mössbauer-spectra-analysis done via NORMOS-SITE-program [47], assuming two-overlapping-sextets representing tetrahedral-A,B-octahedral sites, along with non-magnetic-doublet. Coercivity(H_c)saturation-magnetization(M_s),anisotropy-constant(K_1),squareness-ratio(M_r/M_s),first--derivative(dM/dH) are obtained at room-temperature by Vibrating-sample-magnetometer(Lakeshore-Model-7410). Dielectric parameters: ε',ε'', tan /[__]]#948; (loss-tangent), σ_{ac} (AC-conductivity) of pellets (10 mm diameter) as the dielectric medium, were measured in frequency-range 100Hz-1MHz by Agilent-Technologies-LCR-meter-E4980A. Bertaut-method [48] provides cationic-arrangement, by matching obtained-calculated-intensity-ratio from (422),(400),(200)-planes. This approach reveals how cations are distributed across the A, B sites. It is acknowledged that the Bertaut analysis provides an estimate of cation site occupancy based on XRD intensity ratios; more definitive site-occupancy determination would require neutron diffraction, Mössbauer quantitative fitting, or XAS. In the present work, Mössbauer spectroscopy provides complementary support for the cation distribution model by confirming hyperfine parameters at A and B sites. Optimal cationic-distribution on A,B sites, determined by aligning theoretical-experimental-intensity-ratios is used to get theoretical-magnetization($M_{s(th)}$) at 0 K or Néel-magnetic-moment(n_N) [43]. Formulae [33,34,49,50] used for calculation of structural, magnetic, dielectric parameters are given in the "Supplementary Material".

3. Results and discussions

3.1. Structural analysis

XRD-patterns (Fig. 1(a,b)), and corresponding Rietveld-refined profiles, confirm single-phase-spinel-nanoferrite-formation. Table 2 gives refinement-factors(R-factors);low-goodness-of-fit(GOF)-values show reasonable-refinement-quality revealing structural evolution induced by variation of annealing time. Fig. 1(a) (left-inset) provides magnified view of 311-peak, which reveals peak-shift toward lower-2θ-values,

Table 1
Comparison of the present study with recent literature on annealing-time and annealing-temperature-dependent $MgFe_2O_4$ ferrites.

Study	System	Focus	Key Findings	Difference from Present Work/ Key distinctions	Ref.
Present Work	$MgFe_2O_4$	Annealing time at fixed T = 500°C	Grain growth 25.3–49.3 nm; cation redistribution; enhanced AB/AA, weakened BB exchange; CBH conduction	Fixed-T, variable-time approach; full impedance & Nyquist analysis	—
Tangcharoen (2024)	$MgFe_2O_4$	Annealing temperature	Enhanced ferromagnetism with T	Temperature-variable only; no time-dependent study	[20]
Hussein et al. (2015)	$MgFe_2O_4$ (EDTA sol-gel)	Structure & magnetics vs. T	Ms and Hc tuning with calcination T	Different synthesis; no dielectric/ impedance analysis	[21]
Khirade et al. (2020)	Mg-Zn ferrite	Ceramic vs. sol-gel route	Physical properties comparison	No time-variable annealing; no Mossbauer	[88]
Irfan et al. (2024)	$Cd_{0.55\times}Mg_{0.5}Znx Fe_2O_4$	Zn/Cd substitution	n-doped Cd-Mg spinel properties	Composition-variable, not time-annealing	[39]
Kane et al. (2025)	$MgFe_2O_4$	Annealing temperature	Temperature-driven structural/dielectric changes	Temperature-variable; no fixed-T time study	[41]

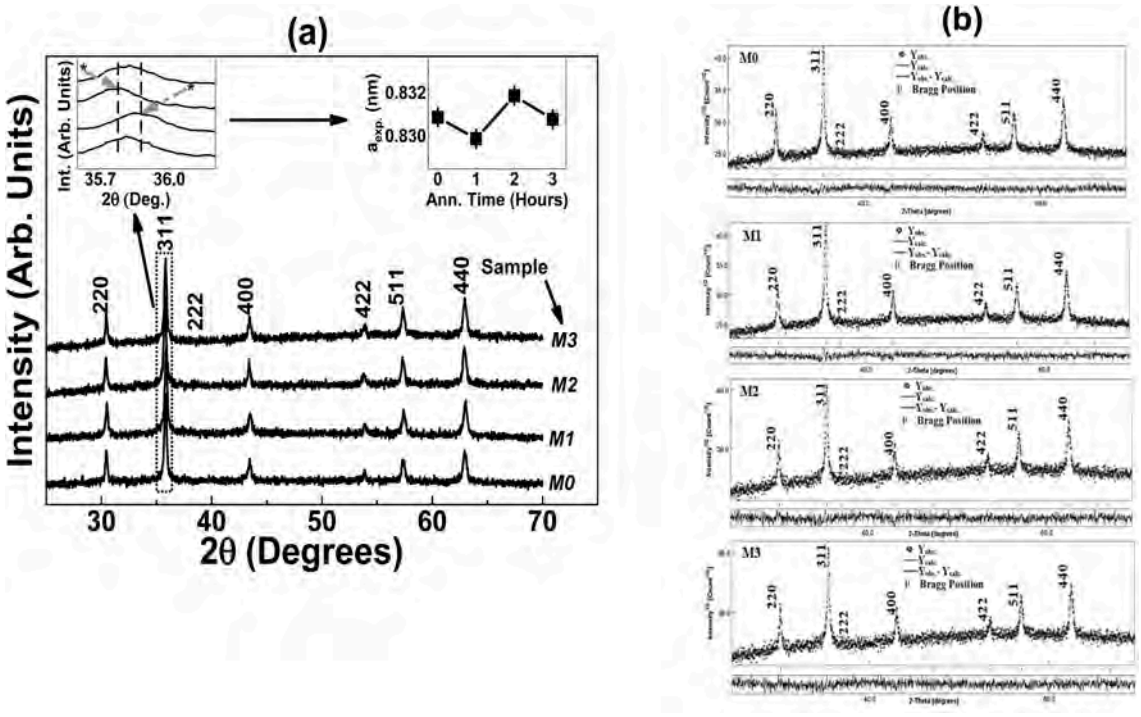

Fig. 1. (a) XRD-Patterns, with the inset showing: (left panel) a zoomed-in view of the 311 reflection, highlighting the peak shift, and (right panel) the annealing time dependence of the experimental lattice parameter (a_{exp}) (**b**) Rietveld-refined-XRD-patterns.

Table 2
Rietveld refinement R parameters, (R_P:Profile-factor,R_{WP}:Weighted-profile-factor,R_{exp}:expected-weighted-profile-factor, goodness-of-fit (GOF).

Sample	R_P (%)	R_{WP} (%)	R_{exp} (%)	GOF
M0	4.70	5.75	3.91	1.47
M1	4.71	5.84	3.87	1.51
M2	3.31	4.19	3.89	1.08
M3	3.28	4.15	3.88	1.07

indicating moderate-increase in lattice-parameter, suggests unit cell-expansion. Lattice-parameter exhibits a non-monotonic-variation (Fig. 1a (right inset)), initially decreasing for the sample corresponding to the treatment for one hour before approaching increasing values for samples annealed for longer durations. These fluctuations in lattice parameter are attributable to a rapid reordering of atoms induced by the thermal annealing process, as was also reported earlier [50,51]. Additionally, it should be noted that the modification (creation or annihilation) of oxygen vacancies during annealing can significantly influence the lattice response: the formation of oxygen vacancies is likely to induce lattice-dilation (e. g. - due to bond weakening and reduced electrostatic interactions etc.), whereas their extinction promotes lattice contraction by restoring bond strength, and structural compactness. It is also noteworthy that moderate lattice contraction may arise due to stress-relaxation, while lattice dilation can further result from bond weakening associated with defect generation [51]. Average-grain-size-variation (Fig. 2(a)), suggests an increase in annealing time leading to bigger grains. This variation can also impact the lattice parameter, as evidenced by the similar trends observed in both the lattice parameter and grain size with respect to annealing time [51–53]. Observed dislocation- density-variation (inset:Fig. 2(a)) can be attributed to dislocation absorption due to grain boundary movements [54,55]. This corroborates well with dislocation-density-trend with annealing time (Fig. 2(b)), whereas the inset shows the increasing behavior of strain as a function of the duration of thermal treatment. Changes in the strain could be suggestive of; i) variation in the

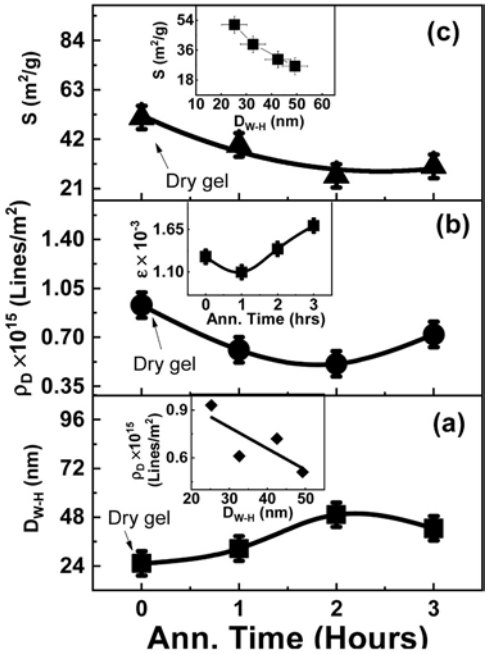

Fig. 2. Annealing-time-dependent:(**a**)D_{W-H}(Inset:ρ_D-D_{W-H})(**b**)ρ_D(Inset:*Strain-ann.-time*) (**c**)S(Inset:*S vs* D_{W-H}).

concentration of lattice imperfections that depends typically on the annealing temperature as well as the time, and ii) growing grains with the time varying isothermal treatment. Overall-grain-growth (Fig. 2(c), inset) induced by annealing, accompanied by decreasing specific-surface-area as isothermal-treatment-duration increases. Fig. 3 demonstrates the trend in bond angles with annealing duration. Bond-angles θ_1,θ_2 give insight into AB interaction: θ_3,θ_4 reflect the BB interaction, θ_5 informs on A-A-interaction [56]. In ferrites,

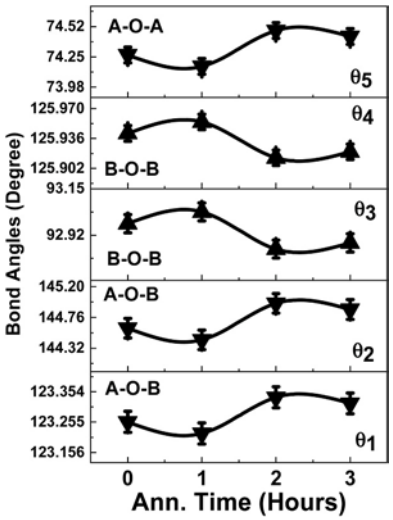

Fig. 3. Variation of Bond Angles with annealing time.

magnetic-link among Mg^{2+}, Fe^{3+} ions occurs through a mediating non-magnetic anion (O^{2-}). Super-exchange-interaction-strength is greatest when bond angle is close to 180° between metal-oxygen-metal, efficiency of interaction depends on both bond-angle, relative distance between magnetic-ions, oxygen [57]. Fig. 3 shows that the bond angles deviate from the ideal 180° value, suggests modified-super-exchange-interactions via reduced-orbital-overlap. For sample treated thermally for one hour, θ_1,θ_2,θ_5-values decrease, while increasing θ_3,θ_4, attributable to lattice-parameter-decrease (Fig. 1(a) right-inset), leading to improved-overlap between oxygen-*p*-orbitals,cation-*d*-orbitals, so reinforcing AB,AA interaction, at the cost of concurrent-weakening of BB-interaction. After a two-hour thermal treatment, the trend reverses i. e. θ_1,θ_2,θ_5 increases, although θ_3,θ_4 decreases, attributable to lattice-parameter-increase (Fig. 1(a) right-inset), which now favors the strengthening of the B-O-B interaction. This may be due to the thermally induced structural modifications as suggested by the Fig. 4(a), associated with the values of oxygen positional parameter *u (which quantifies the structural distortion due to the displacement of oxygen anions*) deviating from its ideal value of 0.375 indicting that oxygen anions are displaced thereby modifying cation–anion bond lengths [1,9]. This shift in the values of (*u*) is due to the migration of cations among the octahedral and tetrahedral sites (see Table 3). Thus cationic redistribution alters the local electrostatic environment thereby affecting the bond angles and hence the super exchange interaction as well. It can be seen in Table 3 that Fe^{3+},Mg^{2+} reside on A,B-sites, though by thermal treatment Mg^{2+} starts to populate B sites and Fe^{3+} on the contrary exhibited a migration to A site which in turn affects net-magnetic-moment of sites A, B suggested by decreasing Neel magnetic moment ($M_{s(th)}$ at 0 K) from 2.4μB to 2μB with the thermal annealing duration as presented in Fig. 4(b).

Fig. 5 depicts EDS patterns, display presence of O,Mg,Fe, weight %, atomic % of the elements is given as inset. Left-panel (Fig. 6) gives SEM images, while right panel (Fig. 6) shows the particle-size-distribution. SEM images given as Fig. 6 (left panel) confirm particle-aggregation, uneven particle-size-dispersal, attributed to magnetic-samples [22,58]. Obtained average-grain-size lie between 103.84 nm to 178.11 nm. Variation of crystallite size among SEM, XRD is attributable to aggregation, due to the magnetic-samples. Distribution-width range between 35 nm to 96.05 nm, is an indicator of the uniformity of the particles, and its lower value reveals less-dispersed particle size.

HRTEM analysis was performed to further elucidate the nanoscale morphology and crystalline structure of the synthesized material by directly visualizing lattice fringes, crystallinity, particle interfaces, and elemental mapping at nanoscale resolution, as demonstrated in recent studies on ferrite nanostructures [59,60]. The HRTEM images, together with the corresponding particle size distribution, and representative (for sample M2) nanoscale elemental maps are presented in Fig. 7, while the Selected Area Electron Diffraction (SAED) indexed patterns and lattice-fringe images are presented in Fig. 8. The particles exhibit a nanoscale morphology with an average crystallite size ranging from 11.7 nm to 24.76 nm, providing complementary confirmation of the nanoscale crystalline nature of the material. The HRTEM images provide direct visualization of well-resolved lattice fringes, with the measured inter-planar spacing corresponding to the characteristic (311) plane of the spinel ferrite structure. The corresponding SAED pattern displays distinct diffraction rings that were indexed to the characteristic crystallographic planes of the spinel phase, further corroborating the XRD results. Furthermore, the elemental maps demonstrate a homogeneous spatial distribution of the constituent elements throughout the examined region, indicating good compositional uniformity without any apparent elemental segregation. Collectively, the agreement among the XRD crystallite size, HRTEM lattice-fringe analysis, SAED indexing, and elemental mapping provides strong evidence for the formation of a well-crystallized and compositionally uniform spinel ferrite phase.

3.2. Magnetic Properties

Hysteresis loops and the corresponding first order derivatives of magnetization (dM/dH) of the samples under study are presented in the Fig. 9(a-c) and corresponding magnetic parameters are depicted in Table 4. It is worth noting that, the observed cation redistribution is consistent with the thermally activated inverse spinel configuration trend observed in Mg-ferrites, where prolonged annealing at elevated temperatures promotes greater inversion. The reduction in Ms(th) from 2.4 μ_B to 2.0 μ_B with increasing annealing duration arises because Mg^{2+} (non-magnetic) displacing Fe^{3+} (magnetic, 5 μ_B) at the B-site reduces the net B-sublattice magnetic moment, thereby lowering the overall Néel moment according to the ferrimagnetic two-sublattice model ($n_N = |M_B$

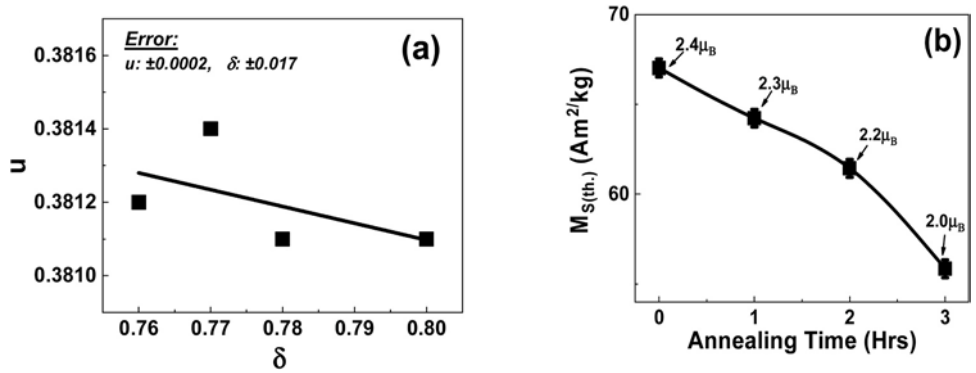

Fig. 4. (a) Plot of u with δ, (b) Annealing-time dependence of $Ms_{(th.)}$ at 0 K.

Table 3
Cationic-distribution, calculated (c)-observed(o) intensity-ratios.

Samples $MgFe_2O_4$	A-site B-site		I_{220}/I_{440}		I_{400}/I_{422}		I_{220}/I_{400}	
			c	o	c	o	c	o
M0	$(Mg^{2+}_{0.24}Fe^{3+}_{0.76})$	$[Mg^{2+}_{0.76}Fe^{3+}_{1.24}]$	0.9271	1.0438	2.1836	2.0923	1.5314	1.6240
M1	$(Mg^{2+}_{0.23}Fe^{3+}_{0.77})$	$[Mg^{2+}_{0.77}Fe^{3+}_{1.23}]$	0.8943	0.9587	2.1410	2.1866	1.5846	1.6401
M2	$(Mg^{2+}_{0.22}Fe^{3+}_{0.78})$	$[Mg^{2+}_{0.78}Fe^{3+}_{1.22}]$	0.7852	0.8233	2.0805	2.1036	1.3820	1.3597
M3	$(Mg^{2+}_{0.20}Fe^{3+}_{0.80})$	$[Mg^{2+}_{0.80}Fe^{3+}_{1.20}]$	0.7189	0.7537	1.9831	2.1126	1.4492	1.3359

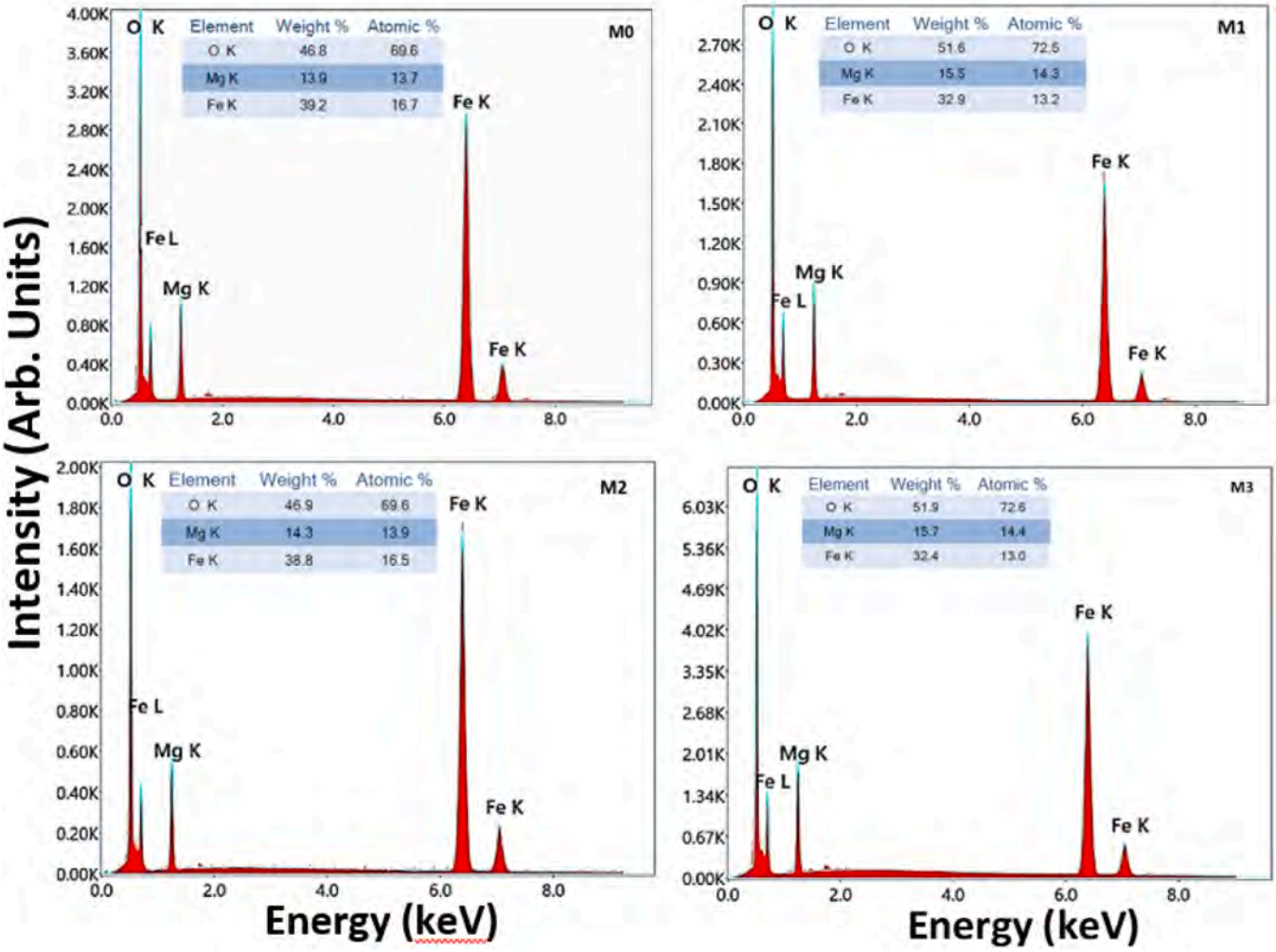

Fig. 5. EDS spectra of the studied samples.

$- M_A|$). This interpretation is consistent with earlier reports on ferrite systems prepared via sol-gel route [61,62]. The double peak behavior observed in the first derivative curves indicates that the hysteresis response of the studied samples results from the competition between exchange interactions and dipolar interactions occurring between the nanograins [63]. Width of first derivative curves shown in Fig. 9(c) varies between 607.45 – 633.02 Oe. These lower values of FWHM are indicating that the studied samples have a uniform particle size [63,64]. Switching field distribution (SFD) values for the studied samples were determined by using the ratio of FWHM values to the corresponding experimentally observed coercive field. SFD values for the samples under study varies between 6.25 and 6.35 as shown in Table 5. The smaller variation in SFD values suggests that the samples have a uniform particle size distribution, meaning there is relatively less variation in the sizes and shapes of the nanoparticles [64,65].

Fig. 10 (a) illustrates the effect of the annealing time on the saturation magnetization response of the samples under investigation, where upper right inset indicates the variation of $M_{s(th)}$ with annealing time and lower inset represents the changes in spin canting angle ($\alpha_{Y\text{-}K}$: Yafet-Kittle angle, obtained from structural data) as a function of the duration of thermal treatment. Experimentally observed magnetization behavior and finite values of spin canting angle ($\alpha_{Y\text{-}K}$) indicates that response of magnetization is administered by Y-K three-sub-lattice-model [66–70] as depicted in Fig. 10 (b). Quantitatively, the Y-K angle increases from approximately 27° to 35° with increasing annealing time, reflecting the growing influence of non-collinear spin alignment at the B-site. This non-collinear arrangement arises because, as more Fe^{3+} ions occupy the A-site with annealing time, the A-B super-exchange interaction strengthens, imposing greater canting on B-site spins. Concurrently, the growing dead-layer thickness (Table 4) further suppresses the net magnetization, as the disordered surface shell does not contribute to long-range magnetic ordering [67–70]. Fig. 11 (a)

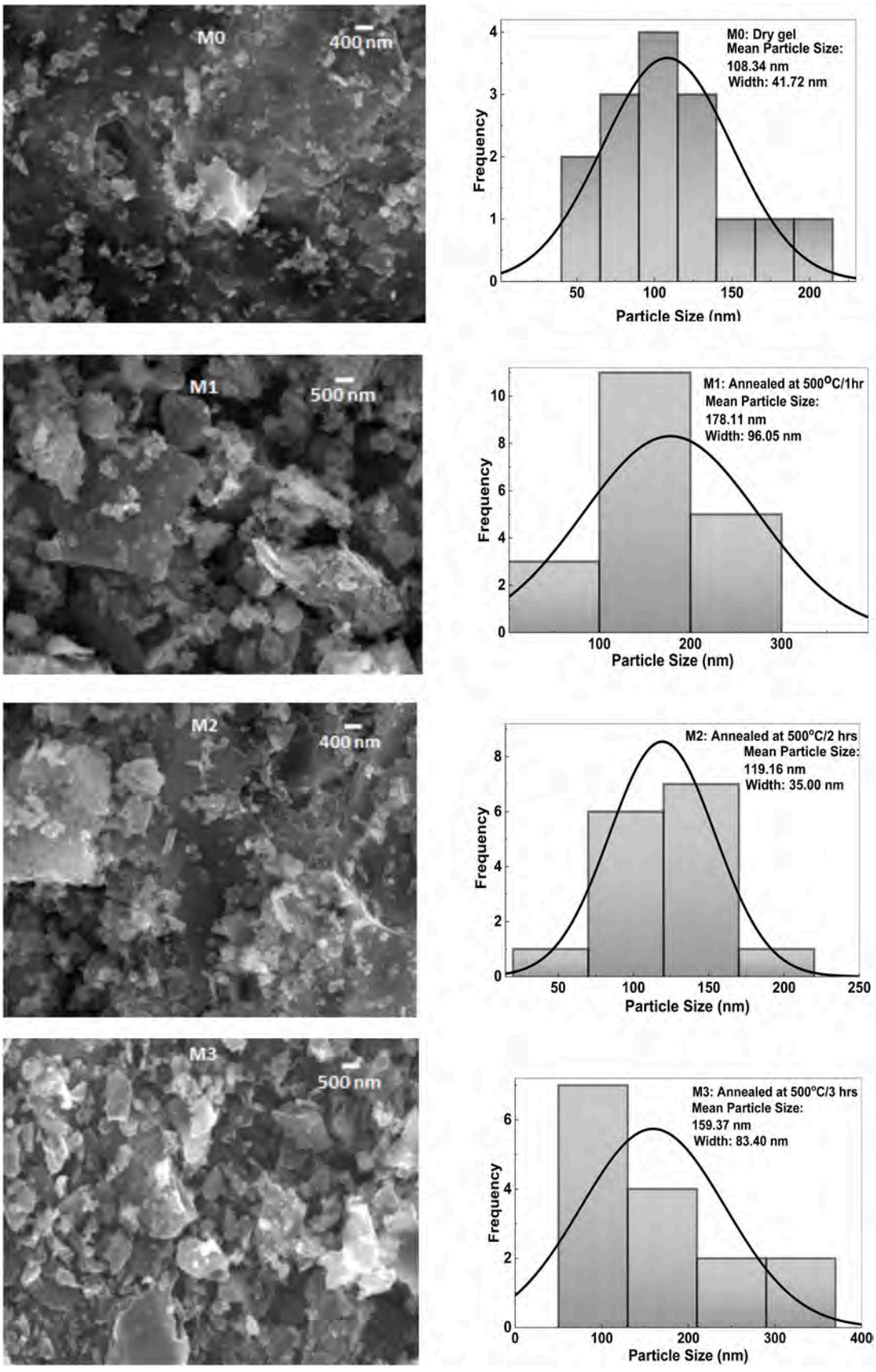

Fig. 6. (Left panel): Scanning Electron Micrographs (Right Panel): respective particle size distribution.

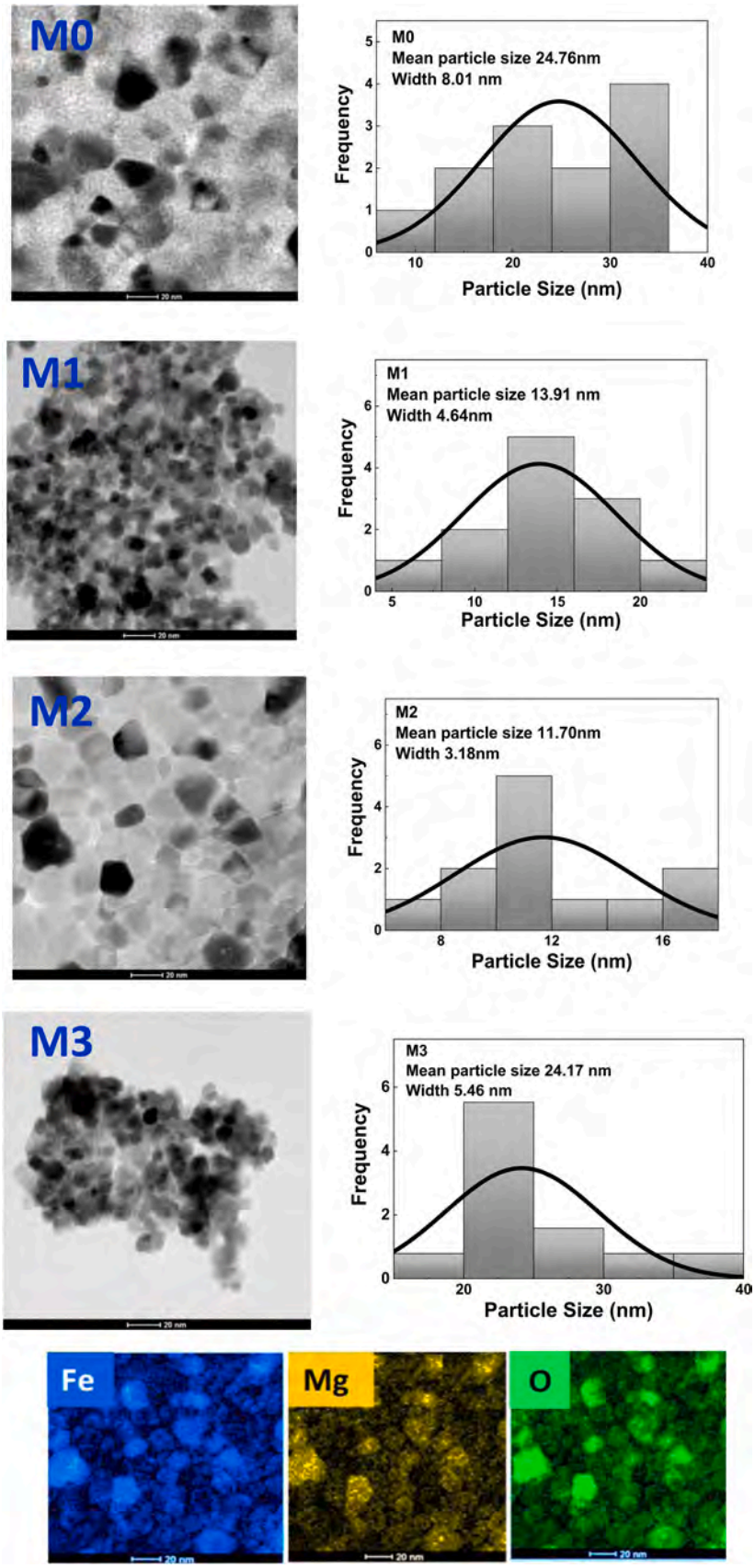

Fig. 7. HRTEM images, corresponding particle size distribution for the studied samples and representative nano-scale elemental maps for M2 sample.

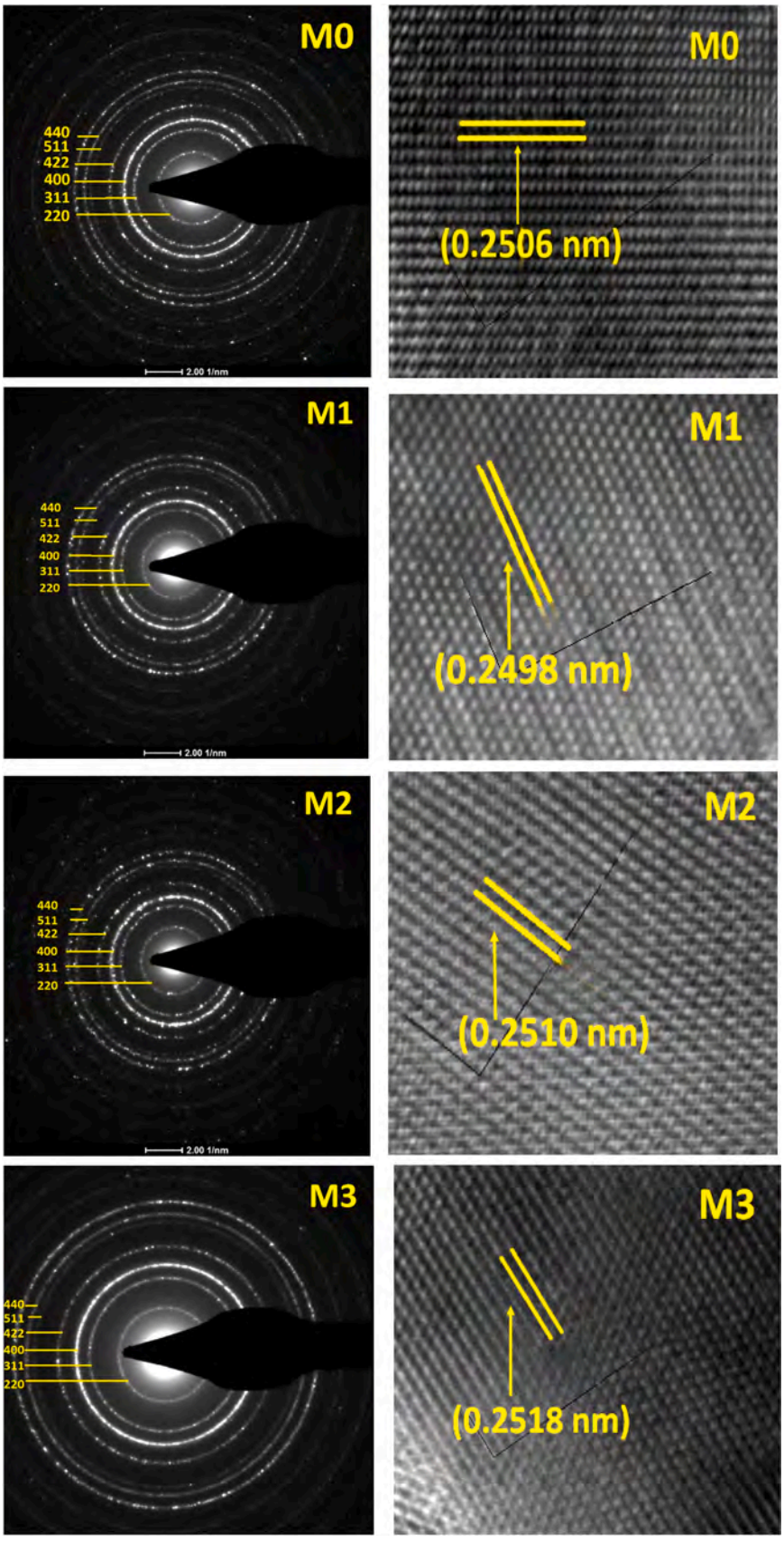

Fig. 8. SAED patterns and measured inter-planar spacing from HRTEM analysis.

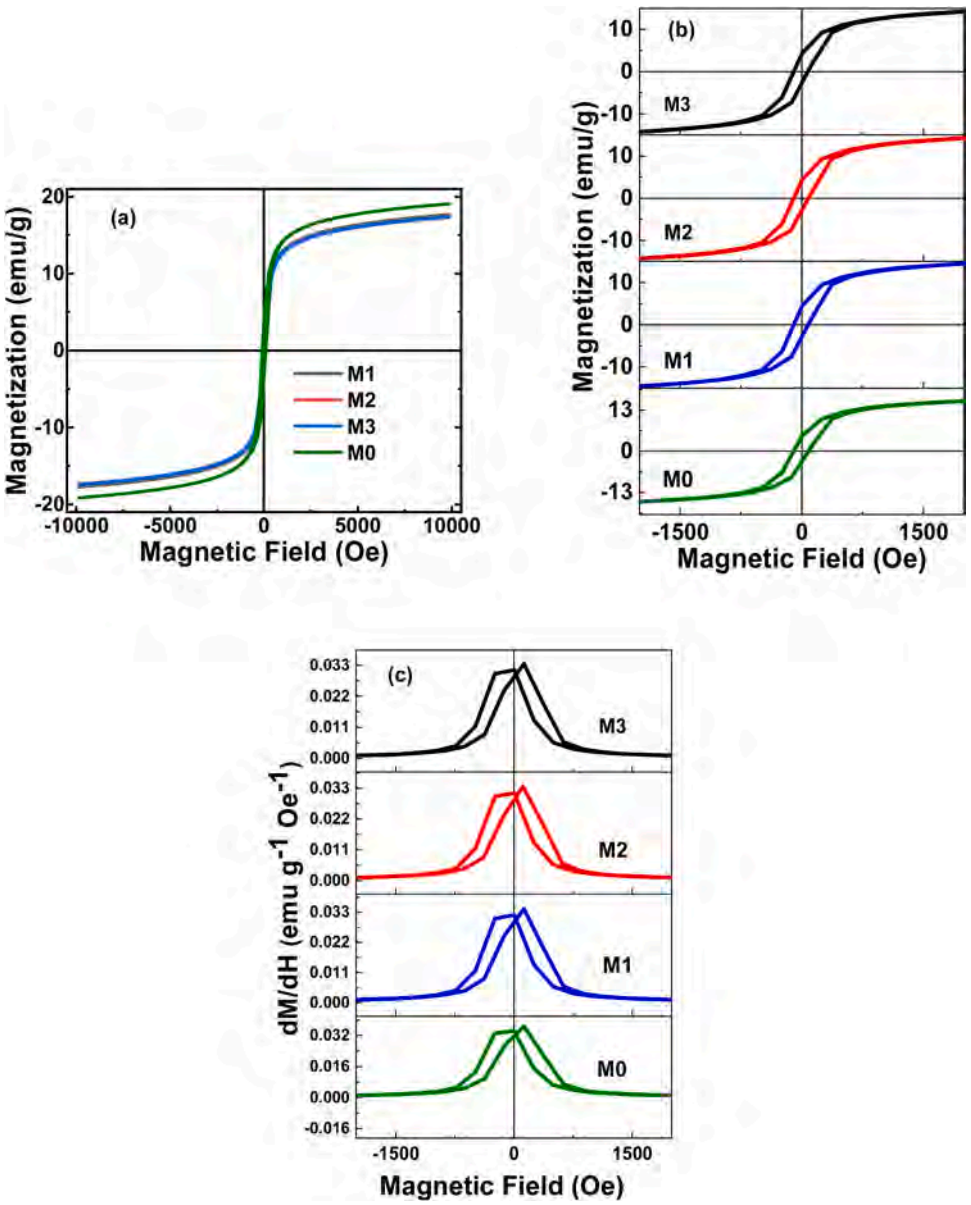

Fig. 9. Hysteresis-loops (a,b), (c) Corresponding first derivatives.

Table 4
Variation of Magnetic Properties with the duration of annealing.

Sample	H_c (Oe) (±2)	$M_{s(exp.)}$ (Am^2/kg) (±0.5)	$M_{s(th.)}$ (Am^2/kg) (±1)	M_r (Am^2/kg) (±0.02)	$K_1(\times 10^3)$ (erg/cc)	M_r/M_s	Dead Layer Thickness t (nm) (±0.5)
M0	100	19.1	67	4.67	8.94	0.246	3.0
M1	98	17.7	64	4.26	8.22	0.241	4.0
M2	97	17.7	61	4.15	8.12	0.234	6.1
M3	97	17.2	55	4.13	7.89	0.239	5.3

Table 5
Switching field distribution (SFD) values for the studied samples.

Samples $MgFe_2O_4$	H_C (Oe) (±2)	FWHM or ΔH of 1st derivative (Oe)	SFD (ΔH/H_C)
M0	100	633.02	6.34
M1	98	609.66	6.23
M2	97	607.45	6.25
M3	97	609.48	6.30

illustrates the magnetization variation with dead- layer, (inset: $M_{s\,(exp)}$–average-grain-size). Inset of Fig. 11 (a) shows that annealing time strongly influences the structural parameters governing the magnetic properties of the system under study. Fig. 11 (b) shows pictographic illustration of core–shell structure of nanoferrite, where these is: i) inner core with parallel or ordered spin-arrangement; ii) surface (or shell) having disordered spins, although core-spin-canting cannot be ruled out [68–74]. It is interesting to observe that while spin canting decreases with increasing annealing time which should enhance the saturation magnetization; but the magnetization actually decreases. This is due to

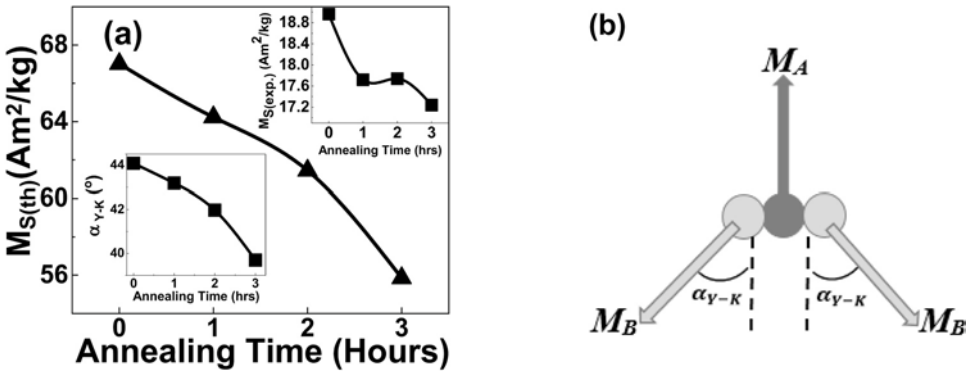

Fig. 10. (a) Annealing time correlation of $M_{s(th)}$, Yafet-Kittle angle (lower inset): and $M_{s(exp)}$ (upper inset) (b) Schematic of non-linear Y-K type magnetic ordering.

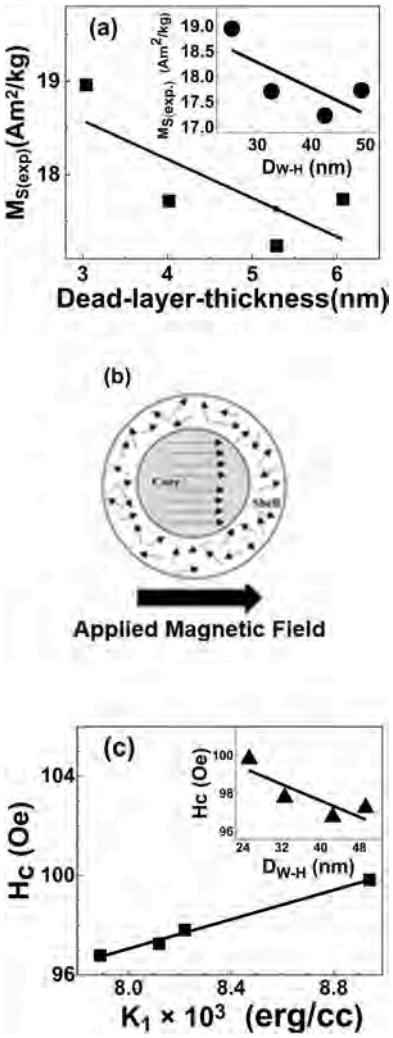

Fig. 11. (a) $M_{s(exp)}$ v/s Dead layer thickness (Inset: variation of $M_{s(exp)}$ v/s average size of nano-grains. (b) Core Shell Structure of nano-grain with dead layer (c) H_c v/s Anisotropy constant (Inset: H_c as a function of average crystallite/grain size).

the increased structural disorder induced spin swaying at the surface (shell) of the nanograins, (see Fig. 11 (b)) as indicated by the growing dead layer thickness (see Table 4), is responsible for monotonic decrease in saturation magnetization values [68–74].

Table 4 indicates that with increasing annealing time the coercive field (H_c) values decreases ascribable to the decrease in the anisotropy constant (K_1) values (Fig. 11(c)). Specifically, K_1 decreases from 8.94 × 10^3 to 7.89 × 10^3 erg/cc as the annealing time increases from 0 to 3 h. This reduction in K_1 is attributed to defect-induced weakening of spin–orbit coupling along with surface-related effects, and is consistent with the softening magnetic behavior reported earlier for ferrites [62]. The reduction in anisotropy constant is also, ascribable to the displaced oxygen anions from their ideal position, leading to expansion of tetrahedral 'A', and concurrent reduction of octahedral 'B' site. Inset of Fig. 11(c) presents coercivity variation with average grain size. Coercivity variation with average grain size shows its reduction with increasing grain size. Coercivity decreases with increasing grain size, as described by the inverse dependence of coercivity on particle diameter [71–75], is consistent with the reduction in anisotropic behavior of nanograins owing to the behavior similar to that of multi domain particles with reduced magnetostatic interaction. This is further supported by values of remanance to saturation magnetization ratio ranging between 0.234 and 0.246 [73–75]. It should be noted that spinel ferrites generally exhibit long-range ferrimagnetic ordering; however, the present disorder (*u parameter varies as 0.3811 – 0.3814, higher than ideal value:0.375, shows higher-disorder in spinel-structure*), including oxygen vacancies, can give rise to localized short-range magnetic correlations [73,74]. This reduction lowers the energy barriers for spin reorientation, thereby enabling relatively stronger effective magnetic interactions among neighbouring grains, without majorly improving the intrinsic long-range magnetic order [73,74].

3.3. Mössbauer analysis

Fig. 12 depicts Mössbauer spectra, for the studied samples, Table 6 gives fitted hyperfine parameters. Based on the literature, the sextet observed in the spectra with the higher-internal-field, attributed to A-site (indicated using red), while lower value corresponds to B-site (shown in blue) [75,76]. The observed isomer shift, which indicates a Fe-ion in the oxidation state of 3 + for all the samples, aligns with previous studies [9]. The progressive increase in the area fraction of sextet-2 (B-site) from 40% (M0) to 53% (M3), alongside the decrease in sextet-1 (A-site) from 37% to 25%, provides direct spectroscopic evidence of the annealing-time-driven cation redistribution inferred from the Bertaut analysis. This cross-validation of structural and Mössbauer data strengthens the proposed cation distribution model. Additional non-magnetic-component characterized by a doublet (depicted in green in Fig. 10) identified with a quadruple-splitting range: 0.61–0.69 mm/s, doublet-area∼ 23%. This observation is ascribable to the shell region characterized with disordered spins (see schematic in Fig. 11 (b)) which does not contribute to the magnetization. One of the important underlying outcomes of this study is as follows: XRD confirms the presence of spinel phase, while Mössbauer being local probe technique, it very clearly detects presence of both spinel phase, as well as a non-magnetic phase. Thus, combined XRD, Mössbauer, magnetic measurements, offer

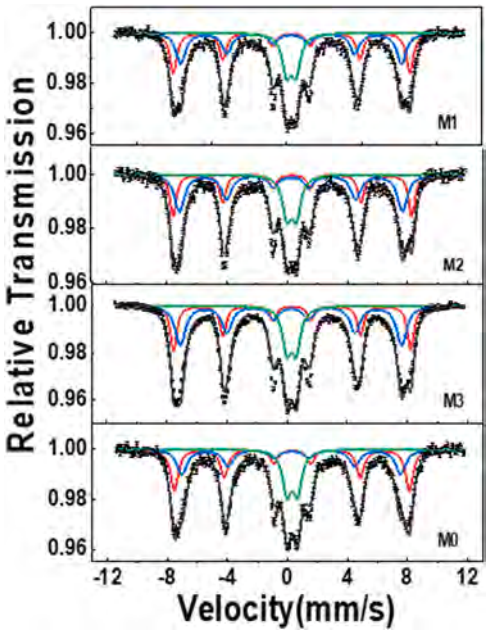

Fig. 12. Fitted Mossbauer-spectra.

Table 6
Fitted Mossbauer-parameters(Width:Line-width,I.S.:Isomer-shift,Q.S.–quadrupole-splitting,B_{hf}:Hyperfine-field, %area:sextet/doublet-area).

Sample	Component	Width (mm/s) (±0.02)	IS (mm/s) (±0.01)	QS (mm/s) (±0.02)	B_{HF} (Tesla) (±0.1)	% Area (±2)
M0	Sextet-1(A)	0.61	0.31	–	48.5	37
	Sextet-2(B)	0.83	0.27	–	45.1	40
	Doublet	0.70	0.31	**0.69**	–	23
M1	Sextet-1(A)	0.57	0.32	–	48.8	33
	Sextet-2(B)	0.75	0.28	–	45.5	44
	Doublet	0.70	0.30	**0.62**	–	23
M2	Sextet-1(A)	0.51	0.33	–	49.1	25
	Sextet-2(B)	0.79	0.26	–	45.9	53
	Doublet	0.70	0.30	**0.62**	–	22
M3	Sextet-1(A)	0.51	0.33	–	48.9	25
	Sextet-2(B)	0.80	0.26	–	45.6	53
	Doublet	0.70	0.30	**0.61**	–	22

enhanced insight on thermal-treatment-influence on magnetic properties.

3.4. Dielectric properties

Fig. 13 (a-d) shows frequency-dependent ε',ε",tanδ,σ_{ac}. Fig. 13 (a) illustrates ε' has higher-values, at lower-frequencies of applied electric field, for both dry gel and thermally treated samples. With increasing frequency of the applied field ε' decreases because electric-dipoles are not able to react to changing electric-field. Remarkably dielectric-constant increases with annealing time and the sample annealed for two hours exhibited fairly high values of dielectric-constant. This may be occurring due to thermally facilitated dipole-alignment along electric-field, resulting-in dielectric-constant-increase, can be explained as composite of relatively conductive-nanograins, separated by less-conductive-grain-boundary-regions [77–80]. When an electric field is applied, charge carriers migrate more easily through the conductive grains, accumulating at grain-boundaries. Charge-accumulation at boundaries generates significant-polarization, which in turn enhances the dielectric response of the material [77–80].

The low-frequency dielectric response of studied samples can be strongly affected by moisture adsorbed from the surrounding atmosphere, particularly in the interfacial polarization region. This effect is more significant for the ~30 nm nanoparticles because of their high surface-to-volume ratio. Surface defects and oxygen vacancies can promote the adsorption of hydroxyl (−OH) groups, followed by the formation of additional layers of physically adsorbed water molecules. At low frequencies, these water molecules can respond to the alternating electric field, producing an additional dipolar contribution and thereby increasing the measured real dielectric permittivity (ε′). The adsorbed moisture layer can also provide additional surface conduction through proton hopping between water molecules. This extrinsic proton transport occurs alongside the intrinsic small-polaron hopping between Fe2 + and Fe3 + ions. Consequently, moisture adsorption may increase the low-frequency AC conductivity and dielectric loss (tanδ). Such moisture-dependent dielectric and conduction effects have been reported for related spinel ferrites and functional ceramics [81,82]. A detailed discussion of surface hydration mechanisms can be found in refs. [83–86]. In the present study, all the measurements were therefore performed under ambient conditions at 25^{O}C and controlled relative humidity to minimize moisture-related effects. Nevertheless, future measurements under vacuum or controlled-humidity conditions would be useful for clearly separating the intrinsic Maxwell–Wagner grain-boundary contribution from moisture-assisted surface polarization and conduction.

Fig. 13 (b and c) represents the frequency dependence of ε", tan δ for Mg-nanoferrite samples, which eventually are indicative of electrical-energy-absorption being utilized for dipolar-rotations and corresponding dissipation owing to relaxation process [77–80]. Additionally, the higher values of ε" and tan δ for the sample annealed for 3-hour duration appears to be resulting from increased in-homogeneities that can result in dielectric-loss as reported earlier [87–89].

It can be seen that ε",tanδ exhibited nearly similar change with frequency characterized with slight-absorption, hence observed low-losses at higher-frequencies. This may be ascribable to the situation when applied-frequency outdo that of hopping of the charge carriers [78,79]. Fig. 13(d) shows frequency-dependent σ_{ac}. At lower-frequencies, the σ_{ac} stays nearly steady. However, with increasing frequency, a significant conductivity-increment is observed, that is caused by motion of free-bound charges. At high-frequency, primary-conduction-mechanism governed by charge-carrier-tunneling, and at lower-frequency, conductivity is influenced by slowed-down-charges through conducting-grains, less-conductive-grain-boundary. Grain-boundary offers high-resistance (low-frequencies), which decreases for higher-frequencies, ultimately contributing to an increase in conductivity [33,79–90]. In current samples (*see* Fig. 13*(a, b)*), the values of ε″ slightly exceed than those of ε′, indicating that the dielectric response is predominantly governed by dissipative (*conductive*) mechanism i. e. an enhancement of σ_{ac}. Furthermore, Fig. 13(c) shows that tan δ values exceeding unity confirm the lossy dielectric nature of the system, which is typically associated with charge carrier hopping, space charge polarization, and defect-mediated conduction, that is also an indicative of the effects arising from variations in oxygen vacancy concentration [84–91]. It is well known that oxygen vacancies lead to modification in conductivity behavior by introducing free charge carriers [91]. In order to further establish a quantitative correlation, obtained room temperature conductivity (σ_{ac}) data (Fig. 13 (d)) was fitted using the frequency dependence of conductivity described by Johncher universal dielectric response law described by:

$$\sigma_{total} = \sigma_{dc} + Aw^{s} \quad (1)$$

1st term represents the frequency independent direct current leakage conductivity contribution and 2nd term represents frequency dependent contribution [92]. Table 7 outlines fitted parameters obtained using conductivity data e.g. the value of σ_{dc}, temperature dependent dimensionless parameter *s*, the parameter *A* signifying the polarizability strength and corresponding barrier height W_m calculated using s parameter. The extracted frequency-independent direct current

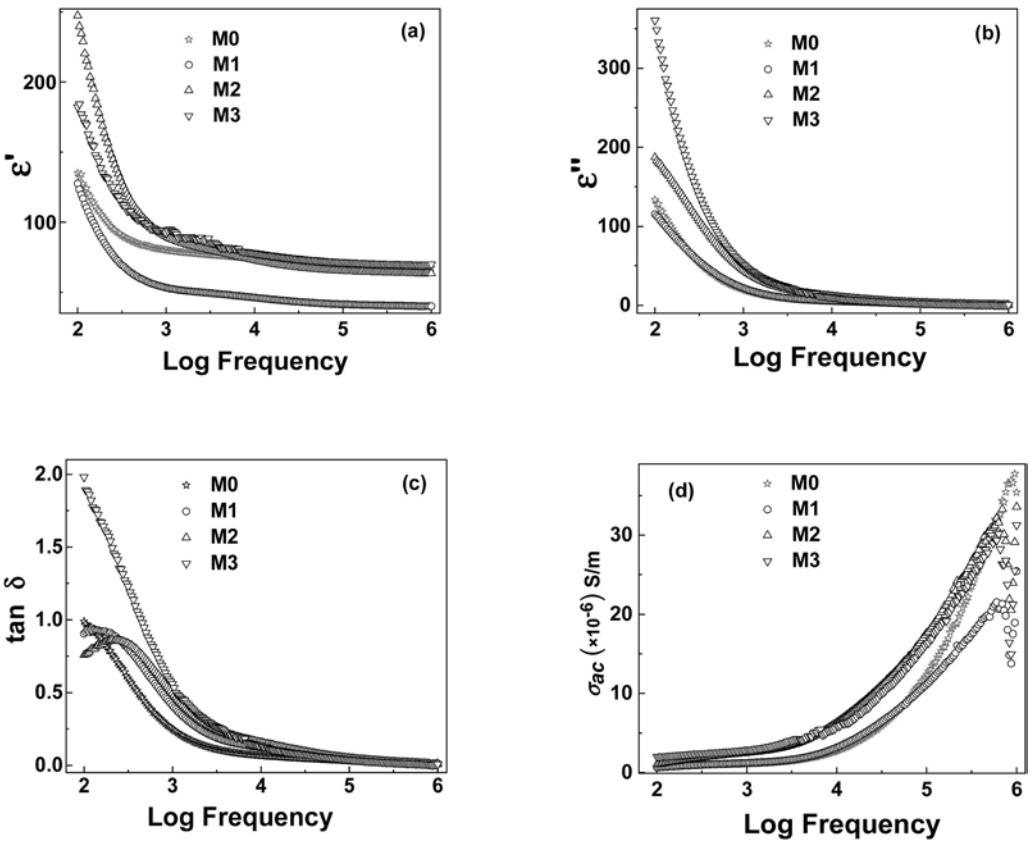

Fig. 13. Frequency dependent thermal-annealing time evolution of:**(a)** ε', **(b)** ε", **(c)** tanδ, **(d)** σ_{ac}.

Table 7
Joncher-power-law fitted/calculated parameters.

Samples	σ_{dc} (S/m)	s	A ($Sm^{-1}rad^{-n}$)	W_m (eV)	V_O^{rel}
M0	3.129×10^{-7}	0.4708	4.9348×10^{-8}	0.2931	1.000
M1	2.246×10^{-7}	0.4232	7.3291×10^{-8}	0.2689	0.7178
M2	4.215×10^{-7}	0.3892	1.7949×10^{-7}	0.2539	1.3470
M3	4.269×10^{-7}	0.3274	3.3325×10^{-7}	0.2306	1.3643

conductivity (σ_{dc}) provides a quantitative measure of the relative oxygen vacancy concentration, as the charge carrier density is directly related to the vacancy concentration according to $\sigma_{dc} = 2q\mu[V_O^{\bullet\bullet}]$ [91]. As all samples were subjected to annealing at the same temperature, the carrier mobility (μ) can be assumed to remain unchanged across the series. Therefore, variations in σ_{dc} can be attributed primarily to changes in oxygen vacancy concentration with annealing duration. This enables σ_{dc} to be used as a reliable quantitative indicator of annealing time dependent relative oxygen vacancy levels, defined as the vacancy concentration in treated samples (M1, M2, M3) normalized to that of the untreated sample (M0). Relative vacancy levels (V_O^{rel}) thus calculated are also shown in Table 7. Upon initial treatment (for 1 h), σ_{dc} decreases markedly to 2.246×10^{-7} S/m, corresponding to a 28.2% reduction in relative oxygen vacancy levels, which may be attributed to initial lattice relaxation and atmosphere-assisted oxygen vacancy annihilation. However, extending the annealing treatment duration to 2 and 3 h reverses this trend, increasing σ_{dc} to 4.215×10^{-7} S/m and 4.269×10^{-7} S/m, respectively. This corresponds to an increase of approximately 36.4% in relative vacancy levels compared to the untreated baseline sample (M0), suggesting that longer treatment durations promote various competing processes that includes migration of Mg^{2+}ions to B sites (see Table 3) giving rise to localized strain regions which corroborates with the observed XRD measurements indicating increasing strain with annealing time (Inset: Fig. 2(b)). In order to relieve this internal energy system undergoes a stress driven secondary defect generation mechanism such as -reduction across the networks of grain boundaries, which in turn regenerates a higher concentration of oxygen vacancies indicated by 36.4%increase in σ_{dc}. Table 7 also shows that hopping exponent $s(< 0.5)$, consistently increase within the narrow range from 0.3724 to 0.4708 with annealing time duration. This implies that the migration of charge carriers, driven by translational motion, causes correlated barrier hopping to dominate the conductivity in the studied samples [81–90], owing to an increase of available free-charge-carrier-population, attributed to their decreasing binding energies and shorter hopping distances which is further supported by the calculated barrier height that systematically decreases (from 0.2931 to 0.2306 eV) with increasing annealing duration as shown in Table 7 [93, 94]. This decrease in barrier height is suggestive of lowering of hopping relaxation time resulting in greater mobility. In the low-frequency region (~100 Hz), highly mobile charge carriers migrate over longer distances within the grains but become impeded at high-resistance grain boundaries. This conductivity mismatch leads to enhanced Maxwell–Wagner space-charge polarization and charge accumulation at internal interfaces contributing significantly to conduction loss tan δ [78], thus the reduced activation barrier facilitates electron hopping, resulting in increased room-temperature dielectric loss at low frequencies (see Fig. 13 (a-b)).

3.5. Impedance analysis

Fig. 14 (a) shows frequency dependent Z'. It illustrates that for all studied samples, Z' decreases sharply with increasing frequency and becomes nearly constant for higher frequencies, displaying similar values across samples due to the release of trapped charges [41,95–98]. This behavior is directly correlated with the microstructural evolution: as annealing time increases from 1 to 3 h, the grain size grows from 25.3 to

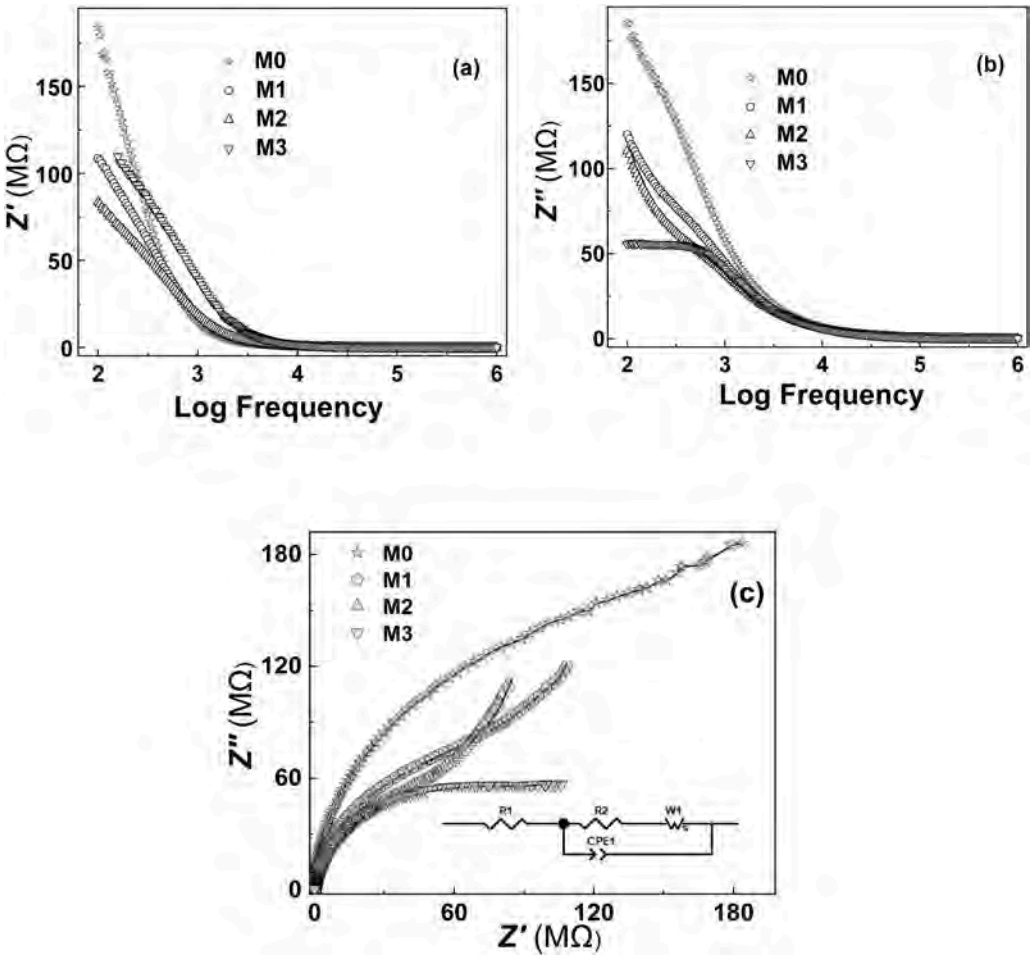

Fig. 14. Frequency-dependence of: (a) Z',(b)Z'',(c) Nyquist-plots (Inset: Equivalent circuit).

49.3 nm accompanied by a corresponding decrease in dislocation density from 0.93×10^{15}–0.51×10^{15} m^{-2} (Fig. 2(a-b)). Larger grains present lower grain-boundary density per unit volume, which reduces the overall grain-boundary resistance (R_{gb} decreases from 255.7 to 92.5 MΩ - see Table 8). Concurrently, dislocation density (Fig. 2(b)) decreases with annealing time, consistent with progressive defect annihilation during isothermal treatment. The combined reduction in grain-boundary resistance and defect density explains the observed decrease in Z′ and Z″ with annealing duration. A similar variation is observed for the frequency-dependent Z″ (figure-14(b)). A noticeable decrease in Z″ at higher frequencies indicates an enhanced shifting of localized charge carriers [89–95]. It appears that as the thermal annealing time was increased, there was a fair step up in the rate of thermally activated charge carrier hopping that has resulted from liberation of confined charge carriers. This is mainly due to defect-reduction in growing grains, polarization associated with accumulated-charges at interfacial grain boundary region [41,94–98]. It is worth noting that interestingly, at the final annealing stage, the impedance continues to decrease despite a partial reversal of the structural parameters. The average grain size decreases to 42.52 nm, while the dislocation density increases to 0.72×10^{15} m^{-2} and the lattice micro-strain reaches 1.7×10^{-3}. This apparent divergence suggests that, at prolonged annealing times, the electrical transport is no longer governed solely by grain-boundary characteristics. Instead, the increased lattice distortion and defect concentration are likely to promote the formation of electrically active defects, such as oxygen vacancies, thereby increasing the concentration of mobile charge carriers. The enhanced carrier concentration compensates for the increased defect scattering associated with grain refinement, resulting in a sustained decrease in both Z′ and Z″. This interpretation is further supported by the concurrent increase in dc conductivity observed for the same sample (Table 7), indicating that defect-assisted hopping conduction becomes the dominant transport mechanism for the studied samples. Fig. 14(c) represents Nyquist-plots depicting the dependence of $Z''$with Z' for dry-gel, annealed-samples. Zview software was used to fit these curves by taking an equivalent circuit that models the resistive-capacitive behaviors of nanograins, grain-boundaries depicted as inset of Fig. 14(c). Electrical-parameters of equivalent-circuit model (Table 8) using a resistive and constant phase element (representative of deviation from an ideal capacitive behavior) network including a Warburg impedance element were used to fit the impedance response. Table 8 presents the fitted equivalent-circuit parameters: grain resistance (Rg), grain-boundary resistance (R_{gb}), CPE parameter (Q), and Warburg impedance (W_R). With increasing annealing time, R_{gb} decreases progressively from 255.7 MΩ (M0) to 92.5 MΩ (M3), while R_g initially increases (2.818–6.449 kΩ) before slightly decreasing for M3 (5.942 kΩ), reflecting competing effects of grain growth and defect annihilation. This progressive improvement in charge transport confirms that grain

Table 8
Equivalent-circuit:R_g–Grain-resistance,R_{gb}-Grain-boundary-resistance,Q–CPE-parameter,W_R–Warburg-Impedance parameters.

Sample	R_g(kΩ)	R_{gb}(MΩ)	Q(pF)	W_R(MΩ)
M0	2.818	255.7	3.073	363.4
M1	5.276	133.8	4.085	755.9
M2	6.449	92.4	4.379	708.4
M3	5.942	92.5	3.810	328.9

boundaries constitute the dominant contribution to electrical resistance and that annealing time is an effective parameter for tailoring the grain-boundary-controlled electrical response of $MgFe_2O_4$ nanoferrites. Perusal of the plots presented in Fig. 14 (c) is suggestive of dispersive-type behavior rather-than semicircle, indicates characteristic non-Debye-type-relaxation-response [41,94–98]. As it can be seen in the plots that the arcs are appearing almost inclined at angles similar to 45^o to the real axis, indicating that diffusion is a predominant mechanism of charge conduction in the studied system. Perusal of Table 8 indicates that the grain boundary resistance parameter is decreasing with annealing-time suggesting released trapped-charges enhancing the conduction process. Increased impedance observed at lower-frequencies indicate conduction limited by diffusion. In contrast, high frequency-impedance-decrease reflects a shift from diffusion-limited-conduction to resistive-tendency [97], as at higher-frequencies, charge-carriers travel easily to electrode, reducing the distance which makes diffusion less-significant, leads to improved-conduction [41,94–98]. Thus present study, through impedance analysis, clearly underscores the significant-contribution of grain-boundaries to the overall electrical conduction. Importantly, it reveals that resistance offered by grain-boundaries decreases with increasing duration of thermal treatment, indicating a progressive improvement in charge-transport across the microstructural interfaces between grains, grain-boundaries.

4. Conclusions

Thermal-annealing-time dependent structural,magnetic,dielectric-response of sol-gel-auto-ignition-synthesized-$MgFe_2O_4$-nano-ferrites are reported. XRD validates creation of nano-crystalline-spinel-phase:grain sizes increasing from 25.3 to 49.3 nm as annealing time progressed. Structural evolution with annealing revealed a non-monotonic change in lattice parameter, grain growth, and enhanced AB,AA super-exchange-interaction, alongside weakened BB exchange, resulting in increased Néel magnetic moment. Cation redistribution, particularly increased Mg^{2+} and decreased Fe^{3+} at the B-site, influenced the oxygen parameter and degree of inversion. The Mössbauer-derived variation in sextet area fractions (B-site area increasing from 40% to 53%) provides direct spectroscopic validation of the cation redistribution model derived from Bertaut analysis. EDS, SEM images respectively establish the presence of Fe,Mg,O, and particle-aggregation, irregular particle-size dispersal Mössbauer spectra show two-magnetic-sextets are associated to Fe^{3+} at A,B-sites, with isomer shifts confirming the +3 oxidation state. A non-magnetic doublet (~23% area) with quadrupole splitting (0.61–0.69 mm/s) was attributed to a disordered shell region, consistent with surface spin disorder. Dielectric analysis showed decreasing $\varepsilon', \varepsilon''$, and tanδ with frequency, while σ_{ac} exhibiting power-law dependence. Comparison with NSPT and QMT models confirms CBH as the dominant conduction mechanism. Impedance results indicated grain boundary-dominated dielectric behavior at high frequencies. Fitted Nyquist parameters confirm R_{gb} decreases from 255.7 to 92.5 MΩ with increasing annealing time, directly quantifying the improvement in inter-granular charge transport.

Overall, the annealing-driven enhancements in magnetic ordering and high-frequency dielectric response position $MgFe_2O_4$ nano-ferrites as promising candidates for microwave electronic and spintronic applications. While the dielectric and magnetic trends presented are indicative of suitability for microwave devices, the authors acknowledge that direct microwave-frequency (GHz range) permeability and electromagnetic absorption measurements are needed for definitive benchmarking. Future work will include these measurements to substantiate the application potential claimed.

CRediT authorship contribution statement

S.S. Modak: Writing – review & editing, Writing – original draft, Formal analysis, Data curation. **P. Tiwari:** Writing – review & editing, Writing – original draft, Software, Methodology, Formal analysis, Data curation. **V.R. Reddy:** Writing – review & editing, Writing – original draft, Methodology, Investigation, Formal analysis, Data curation. **M. Coïsson:** Writing – review & editing, Writing – original draft, Methodology, Investigation, Formal analysis, Data curation. **P. Tiberto:** Writing – review & editing, Writing – original draft, Formal analysis, Data curation. **L. Hashmi:** Writing – review & editing, Writing – original draft, Formal analysis, Data curation. **F. Celegato:** Writing – review & editing, Writing – original draft, Formal analysis, Data curation. **G. Barrera:** Writing – review & editing, Writing – original draft, Methodology, Investigation, Formal analysis, Data curation. **Shailesh I. Kundalwal:** Writing – original draft. **F. Mazaleyrat:** Writing – review & editing, Writing – original draft. **S.N. Kane:** Writing – review & editing, Writing – original draft, Validation, Supervision, Software, Project administration, Methodology, Investigation, Funding acquisition, Formal analysis, Data curation, Conceptualization.

Declaration of generative AI and AI-assisted technologies in the writing process

During the preparation of this work the author(s) used “available versions of Grammarly and QuillBot” in order to “improve its grammar, language, and overall readability of the manuscript”. After using this tool/service, the author(s) reviewed and edited the content as needed and take(s) full responsibility for the content of the published article.

Declaration of Competing Interest

The authors declare that they have no known competing financial interests or personal relationships that could have appeared to influence the work reported in this paper.

Acknowledgements

This work is supported by PAIR-Network of SAKSHAM-funded by ANRF(Anusandhan-National-Research-Foundation), India, through grant-ANRF/PAIR/2025/000018/PAIR, administered and mentored by IIT-Indore.

Appendix A. Supporting information

Supplementary data associated with this article can be found in the online version at doi:10.1016/j.nxmate.2026.103601.

References

[1] J. Smit, H.P.J. Wijn, Ferrites: Physical Properties of Ferromagnetic Oxides in Relation to Their Technical Applications, Philips Technical Library, Eindhoven, 1959.
[2] D.H.K. Reddy, Y.-S. Yun, Spinel ferrite magnetic adsorbents: alternative future materials for water purification? Coord. Chem. Rev. 315 (2016) 90–101, https://doi.org/10.1016/j.ccr.2016.01.012.
[3] T. Harasawa, R. Suzuki, O. Shimizu, S. Ölçer, E. Eleftheriou, Barium-ferrite particulate media for high-recording-density tape storage systems, IEEE Trans. Magn. 46 (2010) 1894–1899, https://doi.org/10.1109/TMAG.2010.2042286.
[4] M. Amiri, M. Salavati-Niasari, A. Akbari, Magnetic nanocarriers: evolution of spinel ferrites for medical applications, Adv. Colloid Interface Sci. 265 (2019) 29–44, https://doi.org/10.1016/j.cis.2019.01.003.
[5] M.D. Shultz, S. Calvin, P.P. Fatouros, S.A. Morrison, E.E. Carpenter, Enhanced ferrite nanoparticles as MRI contrast agents, J. Magn. Magn. Mater. 311 (2007) 464–468, https://doi.org/10.1016/j.jmmm.2006.10.1188.
[6] K. Geetha, R. Udhayakumar, A. Manikandan, Enhanced magnetic and photocatalytic characteristics of cerium substituted spinel MgFe2O4 ferrite nanoparticles, Physica B Condensed Matter 615 (2021) 413083, https://doi.org/10.1016/j.physb.2021.413083.
[7] Q. Jiao, Y. Zhai, X. Bai, W. Zhang, J. Du, H. Zhai, Magnetic properties and induction heating of NiZn ferrite nanoparticles, Mod. Phys. Lett. B 22 (2008) 1497–1503, https://doi.org/10.1142/S0217984908016212.
[8] T. Tatarchuk, B. Al-Najar, M. Bououdina, M.A.A. Ahmed, Catalytic and photocatalytic properties of oxide spinels. Handbook of Ecomaterials, Elsevier, 2018, pp. 1–50, https://doi.org/10.1007/978-3-319-48281-1_158-1.

[9] P. Tiwari, R. Verma, S.S. Modak, V.R. Reddy, S.N. Kane, In-field ^{57}Fe Mössbauer study of $Mg_xZn_{1-x}Fe_2O_4$ prepared by green synthesis method, Hyperfine Interact. 243 (2022) 7, https://doi.org/110.1007/s10751-022-01794-2.

[10] R. Verma, S.S. Modak, A. Ghosh, S.N. Kane, Thermal annealing time assisted modification of structural properties of Mg nano ferrite, AIP Conf. Proc. 2352 (2021) 040006, https://doi.org/10.1063/5.0052432.

[11] A. Daigle, J. Modest, A.L. Geiler, S. Gillette, Y. Chen, M. Geiler, B. Hu, S. Kim, K. Stopher, C. Vittoria, V.G. Harris, Structure, morphology and magnetic properties of $Mg_xZn_{1-x}Fe_2O_4$ ferrites prepared by polyol and aqueous co-precipitation methods, Nanotechnology 22 (2011) 305708, https://doi.org/10.1088/0957-4484/22/30/305708.

[12] P. Manivasagan, S. Ashokkumar, A. Manohar, A. Joe, H.-W. Han, S.-H. Seo, T. Thambi, H.-S. Duong, N.K. Kaushik, K.H. Kim, E.H. Choi, E.-S. Jang, Biocompatible calcium ion-doped magnesium ferrite nanoparticles as photothermal therapeutic materials, Pharmaceutics 15 (2023) 1555, https://doi.org/10.3390/pharmaceutics15051555.

[13] P. Tiwari, S.N. Kane, R. Verma, F. Mazaleyrat, Preparation condition assisted modification of structural and magnetic properties of $MgFe_2O_4$ nanoferrite, AIP Conf. Proc. 2142 (2019) 160003, https://doi.org/10.1063/1.5122326.

[14] G. Sathishkumar, C. Venkataraju, K. Sivakumar, Effect of nickel on the structural and magnetic properties of nanostructured $CoZnFe_2O_4$, J. Mater. Sci. Mater. Electron. 22 (2011) 1715–1721, https://doi.org/10.1007/s10854-011-0351-8.

[15] T. Prabhakaran, R.V. Mangalaraja, J.C. Denardin, J.A. Jiménez, Effect of reaction temperature on the structural and magnetic properties of nano $CoFe_2O_4$, Ceram. Int. 43 (2017) 5599–5606, https://doi.org/10.1016/j.ceramint.2017.01.092.

[16] Ayesha Shahzadi Noreen, Zia Awais, Amna ur Rehman, Moonis Parveen, Zeesham Ali Khan, Abbas, Sol-gel synthesized Ni–Cu–Fe–Cr spinel ferrite with experimental and computational insights for photocatalytic methylene blue degradation, Physica B Condensed Matter (2026) 418566, https://doi.org/10.1016/j.physb.2023.415245.

[17] Aneeta Manjari Padhan, Sanjib Nayak, Manisha Sahu, Zvonko Jagličić, Primož. Koželj, Hoe Joon Kim, Cationic redistribution induced magnetic properties of Zn2+ substituted $MgFe_2O_4$ spinel ferrite, Phys. B Condensed Matter 668 (2023) 415245, https://doi.org/10.1016/j.physb.2023.415245.

[18] G. Barrera, M. Coisson, F. Celegato, S. Raghuvanshi, F. Mazaleyrat, S.N. Kane, P. Tiberto, Cation distribution effect on static and dynamic magnetic properties of $Co_{1-x}Zn_xFe_2O_4$ ferrite powders, J. Magn. Magn. Mater. 456 (2018) 372–380, https://doi.org/10.1016/j.jmmm.2018.02.072.

[19] B. Purnama, A.T. Wijayanta, Suharyana, Effect of calcination temperature on structural and magnetic properties of cobalt ferrite nanoparticles, J. King Saud. Univ. Sci. 31 (2019) 956–960, https://doi.org/10.1016/j.jksus.2018.07.019.

[20] T. Tangcharoen, Enhanced room-temperature ferromagnetism and optical properties of $MgFe_2O_4$ spinel ferrite prepared under different calcination temperatures, Results Mater. 23 (2024) 100596, https://doi.org/10.1016/j.rinma.2024.100596.

[21] S.I. Hussein, A.S. Elkady, M.M. Rashad, A.G. Mostafa, Structural and magnetic properties of magnesium ferrite nanoparticles prepared via EDTA-based sol–gel reaction, J. Magn. Magn. Mater. 379 (2015) 9–15, https://doi.org/10.1016/j.jmmm.2014.11.079.

[22] P. Tiwari, S.S. Modak, A.R. Tanna, S.I. Kundalwal, S.N. Kane, On the comparison of structural properties of as-prepared and thermally treated Mg-Zn nanoferrite powders synthesized via honey assisted sol-gel auto combustion, Research 8 (2026) 101619, https://doi.org/10.1016/j.nexres.2026.101619.

[23] M.L. Hashmi, F.S. Muta, G. Deninno, C. Parmar, R. Verma, F. Mazaleyrat, S. N. Kane, S. Modak, V.R. Reddy, P.M. Tiberto, M. Coïsson, Engineering $MgFe_2O_4$ nanoparticles to enhance magnetic, optical and dielectric performance, J. Magn. Magn. Mater. 641 (2026) 173833, https://doi.org/10.1016/j.jmmm.2026.173833.

[24] M. Naagar, S. Chalia, F. Wan, L.V. Panina, P. Thakur, P.B. Sharma, A. Thakur, Temperature-dependent magnetic properties and thermal stability of $MgFe_2O_4$ nanoparticles, J. Magn. Magn. Mater. 592 (2024) 171798, https://doi.org/10.1016/j.jmmm.2024.171798.

[25] J.P. Singh, R.C. Srivastava, H.M. Agrawal, R. Kumar, V.R. Reddy, A. Gupta, Magnetic study of nanostructured zinc ferrite irradiated with 100 MeV O beam, J. Magn. Magn. Mater. 322 (2010) 1701–1705, https://doi.org/10.1016/j.jmmm.2009.09.068.

[26] J.P. Singh, R.C. Srivastava, H.M. Agrawal, P. Chand, R. Kumar, Size-dependent magnetic resonance in irradiated zinc ferrite nanoparticles, Curr. Appl. Phys. 11 (2011) 532–537, https://doi.org/10.1016/j.cap.2010.09.009.

[27] S.N. Dolia, M.S. Dhawan, A.S. Prasad, S. Kumar, A. Samariya, R.K. Singhal, R. Kumar, Magnetization enhancement in $Co_{0.4}Zn_{0.6}Fe_2O_4$ by Ag^{15+} ion irradiation, Radiat. Eff. Defects Solids 166 (2011) 558–563, https://doi.org/10.1080/10420150.2011.553232.

[28] J.P. Singh, G. Dixit, R.C. Srivastava, H. Kumar, H.M. Agrawal, R. Kumar, Swift heavy ion irradiation effects in nanosized zinc ferrite, J. Magn. Magn. Mater. 324 (2012) 3306–3312, https://doi.org/10.1016/j.jmmm.2012.05.039.

[29] M. Satalkar, S.N. Kane, P.K. Kulriya, D.K. Avasthi, Swift heavy ion irradiated spinel ferrite, Radiat. - Resist. Mater. Nucl. Instrum. Methods Phys. Res. B 379 (2016) 235–241, https://doi.org/10.1016/j.nimb.2016.03.052.

[30] R. Sharma, S. Raghuvanshi, M. Satalkar, S.N. Kane, T.R. Tatarchuk, F. Mazaleyrat, Effect of 120 MeV Si ion irradiation on $NiFe_2O_4$ and $Ni_{0.5}Zn_{0.5}Fe_2O_4$, AIP Conf. Proc. 1953 (2018) 030117 https://doi.org/10.1063/1.5032452.

[31] S. Raghuvanshi, P. Tiwari, S.N. Kane, D.K. Avasthi, F. Mazaleyrat, T. Tatarchuk, I. Mironyuk, Dual control of structure and magnetic properties of Mg ferrite via ion irradiation, J. Magn. Magn. Mater. 471 (2019) 521–528, https://doi.org/10.1016/j.jmmm.2018.10.004.

[32] N.K. Thanh, T.T. Loan, N.P. Duong, L.N. Anh, D.T.T. Nguyet, N.H. Nam, S. Soontaranon, W. Klysubun, T.D. Hien, Cation distribution assisted tuning of magnetization in nanosized magnesium ferrite, Phys. Status Solidi A 215 (2018) 1700397, https://doi.org/10.1002/pssa.201700397.

[33] S.S. Modak, C. Parmar, R. Verma, V.R. Reddy, S.N. Kane, Structural and dielectric properties of $ZnFe_2O_4$: effect of thermal annealing, IOP Conf. Ser. Mater. Sci. Eng. 1316 (2024) 012010, https://doi.org/10.1088/1757-899X/1316/1/012010.

[34] S.N. Kane, C. Parmar, R. Verma, S.S. Modak, V.R. Reddy, Annealing-dependent properties of Ni nanoferrite, in: Multifunctional Materials for Electronics and Biomedical Devices, Springer, 2025, p. 211, https://link.springer.com/chapter/10.1007/978-981-96-7606-4_19.

[35] Sulaiman Al-Sulaimi, M.Qamar Jahan, Mukhtar Ahmad, Zahra Batool, Muhammad Hamza, Atiq ur Rehman, Ghulam Abbas Ashraf, Jin Yang, Essam A. Al-Ammar, Saikh Mohammad Wabaidur, Impact of Zn ferrite and carbon dots on structural, morphological, magnetic properties, Mater. Chem. Phys. 326 (2024) 129721, https://doi.org/10.1016/j.matchemphys.2024.129721.

[36] Komal Farooq, M. Irfan, Majid Niaz Akhtar, Raqiqa Tur Rasool, Mustafa Mahmoud, Abdullah Almohammedi, Ghulam Abbas Ashraf, Muhammad Azhar Khan, Chromium-substituted cadmium post-spinel ferrites (part A), Ceram. Int. 50-18 (2024) 33050–33064, https://doi.org/10.1016/j.ceramint.2024.06.119.

[37] Uzma Batool, Muhammad Iqbal Asif, Zeenat Jabeen, Muhammad Asif, Asadullah Dawood, Mukhtar Ahmad, Rizwan Ul Hassan, Atiq ur Rehman, Ghulam Abbas Ashraf, Hisham S.M. Abd-Rabboh, Doniyor Jumanazarov, Farruh Atamurotov, Phongpichit Channuie, $Li_{0.5}Ce_xFe_{2.5-x}O_4$ ferrite, Mater. Chem. Phys. 340 (2025) 130792, https://doi.org/10.1016/j.matchemphys.2025.130792.

[38] Ghulam Mustafa, Muhammad Azhar Khan, Raqiqa Tur Rasool, Haya Alhummiany, Muhammad Arshad, Ghulam Abbas Ashraf, Hisham S.M. Abd-Rabboh, M. Irfan, Ali S. Alshomrany, Majid Niaz Akhtar, Cadmium (Cd) substituted $CrCd_xFe_{1-x}O_3$ ferrites, Ceram. Int. 50-18 (part A) (2024) 32398–32411, https://doi.org/10.1016/j.ceramint.2024.06.047.

[39] M. Irfan, Ali Hussain, Raqiqa Tur Rasool, Majid Niaz Akhtar, M.Anas Siddique, Abdullah Almohammedi, Mustafa Mahmoud, Magbool Alelyani, Ghulam Abbas Ashraf, Muhammad Azhar Khan, n-doped Cd–Mg spinel ferrites $Cd_{0.5-x}Mg_{0.5}Zn_xFe_2O_4$, Ceram. Int. 50-16 (2024) 27867–27879, https://doi.org/10.1016/j.ceramint.2024.05.083.

[40] Muhammad Ajmal, M.U. Islam, Ghulam Abbas Ashraf, Muhammad Aamir Nazir, M.I. Ghouri, Ga doping in spinel ferrites, Phys. B 526 (2017) 149–154, https://doi.org/10.1016/j.physb.2017.05.044.

[41] S.N. Kane, S.S. Modak, R. Verma, C. Parmar, P. Tiwari, K. Gehlot, V.R. Reddy, M. Coïsson, F. Mazaleyrat, Thermal annealing temperature evolution of structural and dielectric properties of $MgFe_2O_4$, IOP Conf. Ser. Mater. Sci. Eng. 1340 (2025) 012001 https://doi.org/10.1088/1757-899X/1340/1/012001.

[42] L. Lutterotti, P. Scardi, Simultaneous structure and size–strain refinement by the Rietveld method, Appl. Crystallogr. 23 (4) (1990) 246–252, https://doi.org/10.1107/s0021889890002382.

[43] C. Parmar, R. Verma, S.S. Modak, F. Mazaleyrat, T. Tatarchuk, S.N. Kane, Effect of $^{16}O^{6+}$ ion irradiation on Zn nanoferrites, Mol. Cryst. Liq. Cryst. 767 (2023) 115–124, https://doi.org/10.1080/15421406.2023.2228645.

[44] M. Ghasemi Hajiabadi, M. Zamanian, D. Souri, Williamson–Hall analysis of lattice strain and dislocation density in ZnSe and ZnSe:Cu nanoparticles, Ceram. Int. 45 (2019) 14084–14090, https://doi.org/10.1016/j.ceramint.2019.04.107.

[45] R. Verma, S.N. Kane, P. Tiwari, S.S. Modak, F. Mazaleyrat, Cd content dependent magnetic properties of $Li_{0.5-x/2}Cd_xFe_{2.5-x/2}O_4$ nano-ferrite prepared without post preparation thermal treatment, AIP Conf. Proc. 2142 (2019) 160015, https://doi.org/10.1063/1.5122596.

[46] C.A. Schneider, W.S. Rasband, K.W. Eliceiri, NIH Image to ImageJ: 25 years of image analysis, Nat. Methods 9 (2012) (2012) 671.

[47] R.A. Brand, Improving the validity of hyperfine field distributions from magnetic alloys: Part I: Unpolarized source, Nucl. Instrum. Methods Phys. Res. B 28 (1987) 398, https://doi.org/10.1016/0168-583X(87)90182-0.

[48] E.F. Bertaut, Comptes Rendus Hebdomadaires des Seances de l'Academie des Sciences 230 (1950) 213.

[49] M. Rekaby, Dielectric response and Cole–Cole plot analysis for $(Zn_{0.91}Mn_{0.03}Co_{0.06}O)x/Cu_{0.5}Tl_{0.5}Ba_2Ca_2Cu_3O_{10-\delta}$ diluted magnetic semiconductor/superconductor composites, Appl. Phys. A 126 (2020) 664, https://doi.org/10.1007/s00339-020-03849-z.

[50] M. Pardavi-Horvath, Microwave applications of soft ferrites, J. Magn. Magn. Mater. 215–216 (2000) 171, https://doi.org/10.1016/S0304-8853(00)00106-2.

[51] C. Barada, G. Kimmel, A. Opaliński, S. Gierlotka, W. Łojkowski, Lattice variation as a function of concentration and grain size in MgO–NiO solid solution system, Heliyon 10 (2024) e31275, https://doi.org/10.1016/j.heliyon.2024.e31275.

[52] M. Fernandes, K.R.B. Singh, T. Sarkar, P. Singh, R.P. Singh, Recent applications of magnesium oxide (MgO) nanoparticles in various domains, Adv. Mater. Lett. 11 (8) (2020) 1, https://doi.org/10.5185/amlett.2020.081543.

[53] S. Maitra, J. Roy, 3-Nanoceramic matrix composites: types, processing, and applications, in: Advances in Ceramic Matrix Composites, Elsevier, 2018, p. 27, https://doi.org/10.1016/B978-0-443-18598-4.00034-X.

[54] R.C. Pond, D.A. Smith, On the absorption of dislocations by grain boundaries, Philos. Mag. 36 (1977) 353, https://doi.org/10.1080/14786437708244939.

[55] H. Pan, Y. He, X. Zhang, Interactions between dislocations and boundaries during deformation, Materials 14 (2021) 1012, https://doi.org/10.3390/ma14041012.

[56] S.N. Kane, R. Verma, S.S. Modak, V.R. Reddy, F. Mazaleyrat, Structural, Mössbauer and magnetic study of $Co_{1-x}Zn_xFe_2O_4$ (x = 0.0–0.56) nanoferrites, Hyperfine Interact. 244 (2023) 3, https://doi.org/10.1007/s10751-022-01814-1.

[57] J.B. Goodenough, Magnetism and the Chemical Bond, Interscience-Wiley, New York, 1963.

[58] R. Verma, S.N. Kane, U.P. Deshpande, F. Mazaleyrat, Impact of Cd content on properties of Ni1-xCdxFe2O4 nanoferrites prepared without post-preparation thermal treatment, Mater. Today. Proc. 46 (2021) 2205, https://doi.org/10.1016/j.matpr.2021.03.204.

[59] Junyu Chen, Raqiqa Tur Rasool, Ghulam Abbas Ashraf, Hai Guo, The stimulation of peroxymonosulfate via novel $Co_{0.5}Cu_{0.5}Fe_2O_4$ heterogeneous photocatalyst in aqueous solution for organic contaminants removal, Mater. Sci. Semicond. Process. 157 (2023) 107321, https://doi.org/10.1016/j.mssp.2023.107321.

[60] Qaiser Abbas, G. Murtaza, Nawaz Muhammad, Mohsin Ishfaq, H.M.T. Iqbal, Ali Asad, Ghulam Abbas Ashraf, Muhammad Zahir Iqbal, Structural, dielectric and magnetic properties of (ZnFe2O4/Polystyrene) nanocomposites synthesized by micro-emuslion technique, Ceram. Int. 46 (5) (2020) 5920–5928, https://doi.org/10.1016/j.ceramint.2019.11.045.

[61] Ghulam Abbas Ashraf, Lanting Zhang, Waseem Abbas, Ghulam Murtaza, Magnetic and optical properties of Gd-Tl substituted M-type barium hexaferrites synthesized by co-precipitation technique, Curr. Appl. Phys. 19 (4) (2019) 506–515, https://doi.org/10.1016/j.cap.2019.02.005.

[62] Ghulam Abbas Ashraf, Lanting Zhang, Waseem Abbas, G. Murtaza, Synthesis and characterizations of Al-Sm substituted Ba-Sr M-type hexagonal ferrite nanoparticles via sol-gel route, Ceram. Int. 44 (15) (2018) 18678–18685, https://doi.org/10.1016/j.ceramint.2018.07.096.

[63] A.G. Kolhatkar, A.C. Jamison, D. Litvinov, R.C. Willson, T.R. Lee, Tuning the magnetic properties of nanoparticles, Int. J. Mol. Sci. 14 (2013) 15977, https://doi.org/10.3390/ijms140815977.

[64] S. Kumar, R.R. Singh, P.B. Barman, Rietveld refinement and derivative spectroscopy of nanoparticles of soft ferrites (MgNiFe), J. Inorg. Organomet. Polym. Mater. 31 (2021) 528, https://doi.org/10.1007/s10904-020-01764-7.

[65] S. Kumar, P.B. Barman, R.R. Singh, Estimation and association of structural, elastic and magnetic properties of magnesium–nickel ferrite nanoparticles annealed at different temperatures, Mater. Sci. Eng. B 272 (2021) 115362, https://doi.org/10.1016/j.mseb.2021.115362.

[66] N.S.Satya Murthy, M.G. Natera, S.I. Youssef, R.J. Begum, C.M. Srivastava, Yafet–Kittel angles in zinc–nickel ferrites, Phys. Rev. 181 (1969) 969, https://doi.org/10.1103/PhysRev.181.969.

[67] J.M.D. Coey, Noncollinear spin arrangement in ultrafine ferrimagnetic crystallites, Phys. Rev. Lett. 27 (1971) 1140, https://doi.org/10.1103/PhysRevLett.27.1140.

[68] S.N. Kane, R. Verma, S.S. Modak, V.R. Reddy, F. Mazaleyrat, Effect of thermal treatment on structural, Mössbauer and magnetic properties of Zn nanoferrite, Interactions 245 (2024) 36, https://doi.org/10.1007/s10751-024-01881-6.

[69] J.P. Chen, C.M. Sorensen, K.J. Klabunde, G.C. Hadjipanayis, E. Devlin, A. Kostikas, Size-dependent magnetic properties of $MnFe_2O_4$ fine particles synthesized by coprecipitation, Phys. Rev. B 54 (1996) 9288, https://doi.org/10.1103/PhysRevB.54.9288.

[70] M. George, S.S. Nair, A.M. John, P.A. Joy, M.R. Anantharaman, Structural, magnetic and electrical properties of the sol-gel prepared Li0.5Fe2.5O4 fine particles, J. Phys. D Appl. Phys. 39 (2006) 900, https://doi.org/10.1088/0022-3727/39/5/002.

[71] S.N. Kane, M. Satalkar, Correlation between magnetic properties and cationic distribution of $Zn_{0.85-x}Ni_xMg_{0.05}Cu_{0.1}Fe_2O_4$ nano spinel ferrite: effect of Ni doping, J. Mater. Sci. 52 (2017) 3467, https://doi.org/10.1007/s10853-016-0636-7.

[72] E.C. Stoner, E.P. Wohlfarth, A mechanism of magnetic hysteresis in heterogeneous alloys, Philos. Trans. R. Soc. Lond. A 240 (1948) 599, https://doi.org/10.1098/rsta.1948.0007.

[73] B.D. Culity, C.D. Graham, Introduction to magnetic material, Chapter 11, 2nd edition, John Willey & Sons Inc. Publication.

[74] Stephen Blundell, Magnetism in condensed matter, Chapter 4-6, Oxford University Press.

[75] C.N. Chinnasamy, A. Narayanasamy, N. Ponpandian, K. Chattopadhyay, K. Shinoda, B. Jeyadevan, K. Tohji, K. Nakatsuka, T. Furubayashi, I. Nakatani, Mixed spinel structure in nanocrystalline $NiFe_2O_4$, Phys. Rev. B 63 (2001) 184108 https://doi.org/10.1103/PhysRevB.63.184108.

[76] P. Tiwari, R. Verma, S.S. Modak, V.R. Reddy, F. Mazaleyrat, S.N. Kane, ^{57}Fe Mössbauer study of $CoCr_xFe_{2-x}O_4$ nano ferrite, Hyperfine Interact. 242 (2021) 51, https://doi.org/10.1007/s10751-021-01781-z.

[77] M. Shakir, B.K. Singh, R.K. Gaur, B. Kumar, G. Bhagavannarayana, M.A. Wahab, Dielectric behavior and ac electrical conductivity analysis of ZnSe chalcogenide nanoparticles, Chalcogenide Lett. 6 (2009) 655. https://files01.core.ac.uk/download/34213340.pdf.

[78] K.W. Wagner, Zur Theorie der unvollkommenen Dielektrika, Ann. der Phys. 40 (1913) 817, https://doi.org/10.1002/andp.19133450502.

[79] C.G. Koops, On the dispersion of resistivity and dielectric constant of some semiconductors at audiofrequencies, Phys. Rev. 83 (1951) 121, https://doi.org/10.1103/PhysRev.83.121.

[80] P. Jaita, A. Watcharapasorn, N. Kumar, D.P. Cann, S. Jiansirisomboon, Large electric field-induced strain and piezoelectric responses of lead-free $Bi_{0.5}(Na_{0.80}K_{0.20})_{0.5}TiO_3$–$Ba(Ti_{0.90}Sn_{0.10})O_3$ ceramics near morphotropic phase boundary, Elect. Mater. Lett. 11 (2015) 828, https://doi.org/10.1007/s13391-015-4495-1.

[81] R. Shunmuga Priya, Priyanka Chaudhary, E. Ranjith Kumar, A. Balamurugan, Ch Srinivas, G. Prasad, B.C. Yadav, D.L. Sastry, Evaluation of structural, dielectric and electrical humidity sensor behaviour of MgFe2O4 ferrite nanoparticles, Ceram. Int. 47 (11) (2021) 15995–16008, https://doi.org/10.1016/j.ceramint.2021.02.174.

[82] Mehmet Kuru, Tu.ğba Şa.şmaz Kuru, Ertuğrul Karaca, Sadık Bağcı, Dielectric, magnetic and humidity properties of Mg–Zn–Cr ferrites, J. Alloy. Compd. 836 (2020) 155318, https://doi.org/10.1016/j.jallcom.2020.155318.

[83] Muhammad Junaid, Imrana Kousar, Shagufta Gulbadan, Muhammad Azhar Khan, Muhammad Asif Yousuf, Mirza Mahmood Baig, Ghulam Abbas Ashraf, H. H. Somaily, Manal Morsi, Structural, microstructural, spectral, and dielectric properties of erbium substituted spinel ferrites, Phys. B Condensed Matter 641 (2022) 414120, https://doi.org/10.1016/j.physb.2022.414120.

[84] Qurat Ul. Ain Shahid, Muhammad Azhar Khan, Shagufta Gulbadan, Ghulam Abbas Ashraf, Raqiqa Tur Rasool, Impact of erbium substitution on structural, dielectric, spectral, and microwave absorption properties of $Ba_3Co_2Fe_{24}O_{41}$ Z-type hexa-ferrites for microwave devices applications (Part A), Ceram. Int. 49-17 (2023) 27866–27877, https://doi.org/10.1016/j.ceramint.2023.06.003.

[85] Areeba Iqbal, Muhammad Azhar Khan, Raqiqa Tur Rasool, Shagufta Gulbadan, Mohammed M. Algaradah, Ghulam Abbas Ashraf, Thamraa Alshahrani, Hisham S. M. Abd-Rabboh, Majid Niaz Akhtar, M. Irfan, Dielectric, reflection loss and physicochemical studies of Cr doped Ba–Sr based W type hexagonal ferrites for microwave absorption applications, 50-3-Part A, Ceram. Int. (2024) 4446–4461, https://doi.org/10.1016/j.ceramint.2023.11.163.

[86] Sikandar Hayat, Muhammad Azhar Khan, Raqiqa Tur Rasool, Ghulam Abbas Ashraf, Structural, morphological, XPS, dielectric and spectral properties of sol-gel synthesized Ba–Zn–Cr U-type nanocrystalline magnetic oxide materials, Ceram. Int. 49-19 (2023) 31915–31930, https://doi.org/10.1016/j.ceramint.2023.07.154.

[87] D.M.D.M. Prabaharan, K. Sadaiyandi, M. Mahendran, S. Sagadevan, Structural, optical, morphological and dielectric properties of cerium oxide nanoparticles, Mater. Res. 19 (2016) 478, https://doi.org/10.1590/1980-5373-MR-2015-0698.

[88] S. Suresh, Synthesis, structural and dielectric properties of zinc sulfide nanoparticles, Int. J. Phys. Sci. 8 (2013) 1121, https://doi.org/10.1590/1980-5373-MR-2015-0698.

[89] P.P. Khirade, A.R. Chavan, S.B. Somvanshi, J.S. Kounsalye, K.M. Jadhav, Tuning of physical properties of multifunctional Mg-Zn spinel ferrite nanocrystals: comparative investigations via conventional ceramic versus green sol-gel combustion route, Mater. Res. Express 7 (2020) 116102, https://doi.org/10.1088/2053-1591/abca6c.

[90] F. Kremer, A. Schönhals (Eds.), Broadband Dielectric Spectroscopy, Springer, Berlin, 2003.

[91] P. Kofstad, Nonstoichiometry, Diffusion, and Electrical Conductivity in Binary Metal Oxides, Wiley-Interscience, New York, 1972.

[92] A.K. Jonscher, The 'universal' dielectric response, Nature 267 (1977) 673, https://doi.org/10.1038/267673a0.

[93] V. Chithambaram, S. Jerome Das, S. Krishnan, Synthesis, optical and dielectric studies on novel semi-organic nonlinear optical crystal by solution growth technique, J. Alloy. Compd. 509 (2011) 4543, https://doi.org/10.1016/j.jallcom.2011.01.091.

[94] K.H. Mahmoud, F.M. Abdel-Rahim, K. Atef, Y.B. Saddeek, Dielectric dispersion in lithium–bismuth-borate glasses, Curr. Appl. Phys. 11 (2011) 55, https://doi.org/10.1016/j.cap.2010.06.018.

[95] H. Ali, S. Karim, M.A. Rafiq, K. Maaz, A.U. Rahman, A. Nisar, M. Ahmad, Electrical conduction mechanism in ZnS nanoparticles, J. Alloy. Compd. 612 (2014) 64, https://doi.org/10.1016/j.jallcom.2014.05.163.

[96] M. Younas, M. Nadem, M. Atif, R. Grossinger, Metal-semiconductor transition in $NiFe_2O_4$ nanoparticles due to reverse cationic distribution by impedance spectroscopy, J. Appl. Phys. 109 (2011) 093704, https://doi.org/10.1063/1.3582142.

[97] M.M. Costa, G.F.M. Pires, A.J. Terrezo, M.P.F. Graça, A.S.B. Sombra, Impedance and modulus studies of magnetic ceramic oxide $Ba_2Co_2Fe_{12}O_{22}$ (Co_2Y) doped with Bi_2O_3, J. Appl. Phys. 110 (2011) 034107 https://doi.org/10.1063/1.3615935.

[98] E. Barsoukov, J.R. Macdonald, Impedance Spectroscopy: Theory, Experiments and Applications, Wiley, New York, 2005. ISBN: 0-471-64749-7.